Design and Implementation of an X-by-wire Automotive Prototype

Guillaume Sauze

Department of
Mechanical Engineering
McGill University
Montreal, Canada

March 2015

A thesis submitted to McGill University
in partial fulfillment of the requirements for the degree of
Master of Engineering

2015/03/03

Abstract

The concept of the electric vehicle as a fully automated mobile robot (a.k.a. X-by-wire or drive-by-wire) is becoming more and more attractive in the modern automotive industry. This idea is based on replacing every mechanical subsystem with its electronic equivalent by using sensors, actuators and a computer between them. These alternatives to the mechanical paradigm also constitute the general electronic paradigm. Three of the components, namely throttle-by-wire, brake-by-wire, and steer-by-wire, are the most complex and risky elements amongst those in the X-by-wire technology. In this thesis a new X-by-wire system is proposed and the control for its components is discussed while at the same time emphasizing the steer-by-wire steering mechanism verifying the Ackermann conditions. The proportions of the Toyota Tacoma are used as a benchmark. A scaled-down 3:20 proof-of-concept model was built and tested. The influence of heading velocity and turn angle on the slipping angle and path error is analyzed. The performance of the dynamics of the prototype is discussed, the no-slip assumption is evaluated.

Résumé

Considérer un véhicule électrique comme un robot mobile complétement automatisé (c.f. X-par-câbles ou conduite-par-câbles) devient de plus en plus séduisant pour l'industrie automobile moderne. Ce concept est basé sur l'idée de remplacer chaque système mécanique par son équivalent électronique, en utilisant des capteurs, des actionneurs et un ordinateur placé entre eux. Ces alternatives au paradigme mécanique, en utilisant des composants électroniques, constitutent le paradigme électronique. Trois des composants de ce paradigme, nommés pédales-par-câbles, freins-par-câbles, et direction-par-câbles, sont les plus complexes et les plus risqués. Dans cette thèse, un nouveau système X-par-câbles est proposé, et le dispositif de commande de ses composants est discuté, en mettant l'accent sur le mécanisme de direction-par-câbles, qui vérifie les conditions d'Ackermann. Les proportions de la Toyota Tacoma sont utilisées comme banc d'essai. En effet, un modèle réduit à l'échelle 3:20, démonstrateur de concept, a été construit et testé, pour analyser l'influence de la vitesse de conduite et de l'angle de rotation sur l'erreur de parcours. Enfin, la performance du comportement dynamique du prototype est discutée, et la pertinence de l'hypothèse de non-glissement est évaluée.

Acknowledgements

I would like to express my gratitude to my supervisor, Prof. Jorge Angeles. He helped me to improve my research methods and suggesting other approaches and considerations when I was at an impasse.

I am indebted to Saman Rahimi, a PhD candidate under Prof. Boulet's supervision, who also belongs to the APC Program. Saman's skills and dedication to the project enabled us overcome many technical difficulties. Completing the project would have been much more difficult without his invaluable help. Special thanks to Thomas Friedlaender for providing his scientific insight, suggesting easy-to-use Arduino microcontrollers, thereby allowing me to speed up many technical steps, and helping me to edit this thesis. Mikael Persson, and Prof. Nahon, are due special recognition for spending hours helping Saman and me, especially during the setup of the tests. Moreover, profound thanks to Xiao (Nate) He, who donated a steering wheel controller for the prototype and also machined the plexiglass plate, and to Dr. Zou as well, who very kindly helped me when I was facing difficulties, including writing in LaTeX. I also want to express my sincere gratitude to the APC Project for having had the opportunity to work at the Centre for Intelligent Machines (CIM), at McGill University. Many thanks to my lab colleagues for their kindness and *esprit de corps*. I have wonderful memories of working there.

Last but not least, let me thank my parents, Chantal and Patrick, who are the foundation of my resolve and *sangfroid*, especially when I thought I wouldn't make it to the end. *Merci infiniment !*

Contents

List of Figures

List of Tables

Chapter 1

Introduction

1.1 Background

Automotive vehicles have become widespread since Ford created the first commercial model in 1908, the famous model T. Every part of these vehicles has evolved through the years, always becoming more elaborate and more efficient, from the chassis to the motor. Despite evidence of evolution only one architecture has been widely used so far. Yet recent breakthroughs in electric motors, batteries and electronics have led to alternative architectures that are being researched and tested on a small scale, especially applied to electric vehicles. These technologies seem to be the origins of the future standard fully electronic control architecture, in which stand-alone mechanical parts will be controlled by electronic systems.

1.1.1 Standard Automotive Architecture

In standard architecture there is one main motor providing the torque that propels the automotive vehicle. The motor is connected to a gear box and that connects to a differential mechanism. The gear box reduces the angular velocity from the motor, while the differential mechanism uses the output of the gear box to create two different angular velocities. Most of the time, in rear-drive vehicles, the differential mechanism is connected to the two rear wheels, one transmitted directly to each traction wheel. These angular velocities are different when the automotive vehicle is turning. Several layouts are shown in Fig. 1.1; these include the motor (represented as a rectangle with four small circles inside it), the gear box (pictured as a rectangle with lines inside) and the differential mechanism(s) (circles containing a cross). Subfigures 1.1(a) and (b) correspond to front-drive vehicles, sub-figures 1.1(c) and (d) to rear-drive vehicles and 1.1(e) represents a four-wheel-drive vehicle.

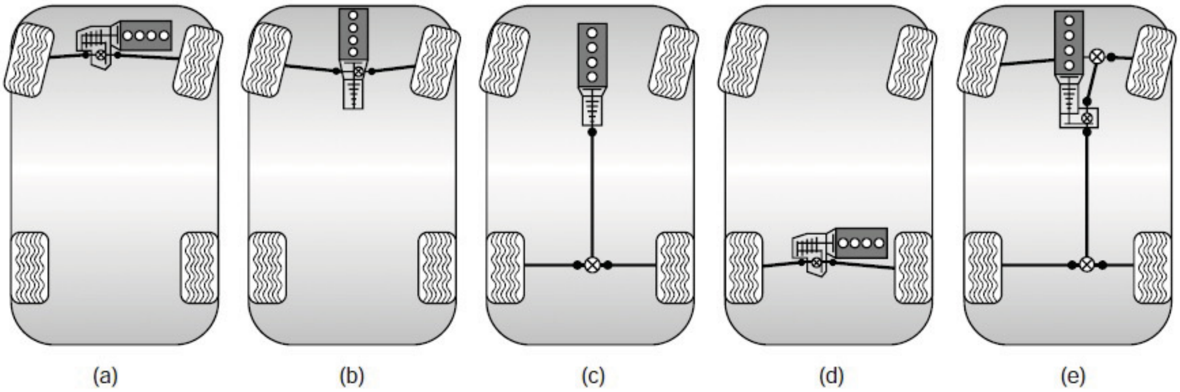

Fig. 1.1 Different layouts of the driveline (Crolla, 2009): (a) and (b) front-wheel-drive; (c) and (d) rear-wheel-drive; (e) four-wheel-drive

Fig. 1.2 and Fig. 1.3 show examples of transmission and differential mechanisms.

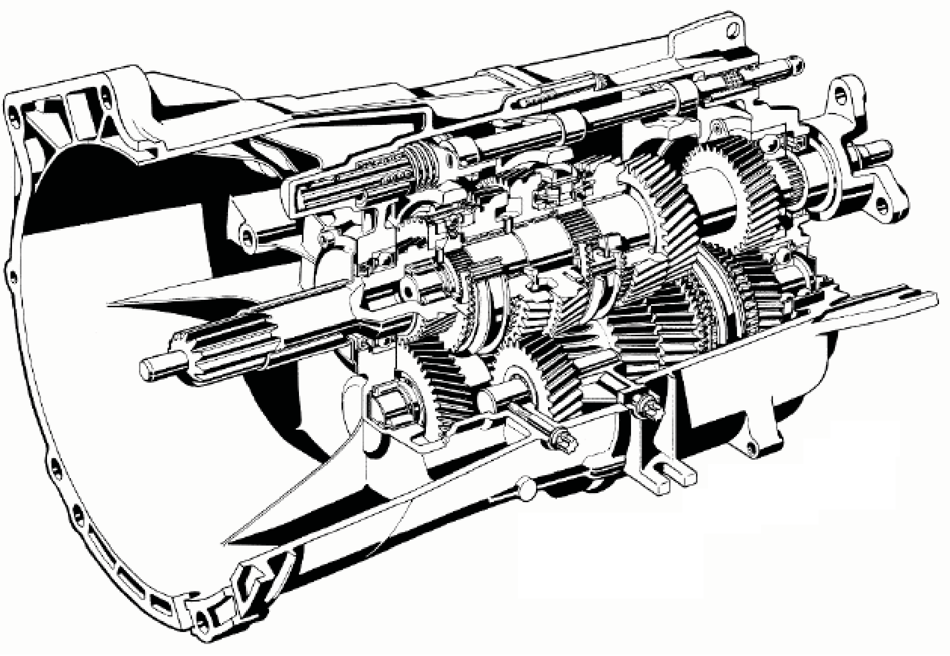

Fig. 1.2 Typical transmission mechanism (Naunheimer, 2011)

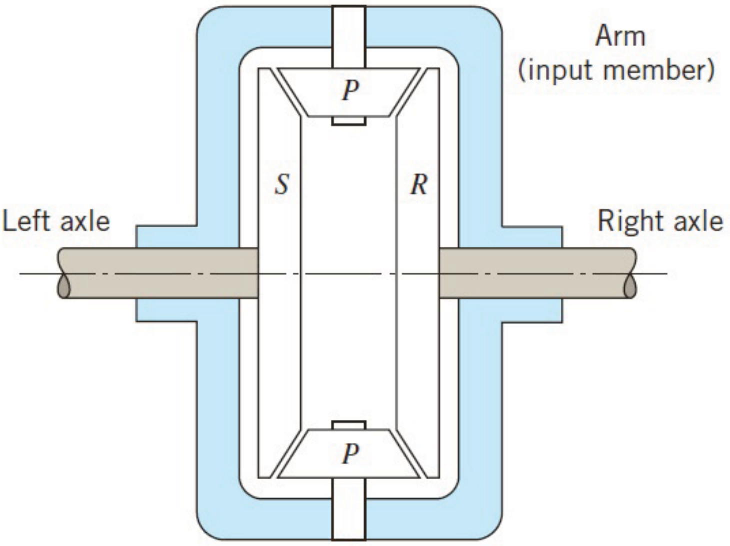

Fig. 1.3 Typical gear differential mechanism (Juvinall and Marshek, 2012)

Depicted in Fig 1.3 is a differential mechanism, whereby S is the sun gear, R the ring gear and P represents the planets. The standard automotive steering system is shown in Fig 1.4 (Wong, 2001), in which the driven wheels are steered via the steering column and the steering mechanism—mechanical systems that are connected to the steering wheel.

Fig. 1.4 Standard steering column and steering mechanism (Crolla, 2009)

1.1.2 X-by-wire

X-by-wire comprises several different technologies: steer-by-wire, throttle-by-wire, brake-by-wire, differential-by-wire, shift-by-wire, suspensions-by-wire and steering-mechanism-by-wire (Seidel, 2009). For any function that used to be implemented via a purely mechanical system and can be replaced by an electronic equivalent, there is a by-wire equivalent. Each by-wire technology provides a new opportunity for research (Kelling and Leteinturier, 2003). The terms “X-by-wire” and “drive-by-wire” are the same and may refer to one or a combination of several by-wire technologies. The suggested architecture, implemented and tested in this thesis, is an X-by-wire architecture using almost all the by-wire technologies mentioned in the subSections below, to create what is therefore called a full X-by-wire architecture. The goal is to substitute every mechanical sub-system by its electronic counterparts.

1.1.3 Steer-by-wire and Steering-mechanism-by-wire

Steer-by-wire is the most popular by-wire technology. Since 2000 extensive research and patents have been published on this topic (Andonian, 2001; Dilger, 2001; Peter and Gerhard, 1999).

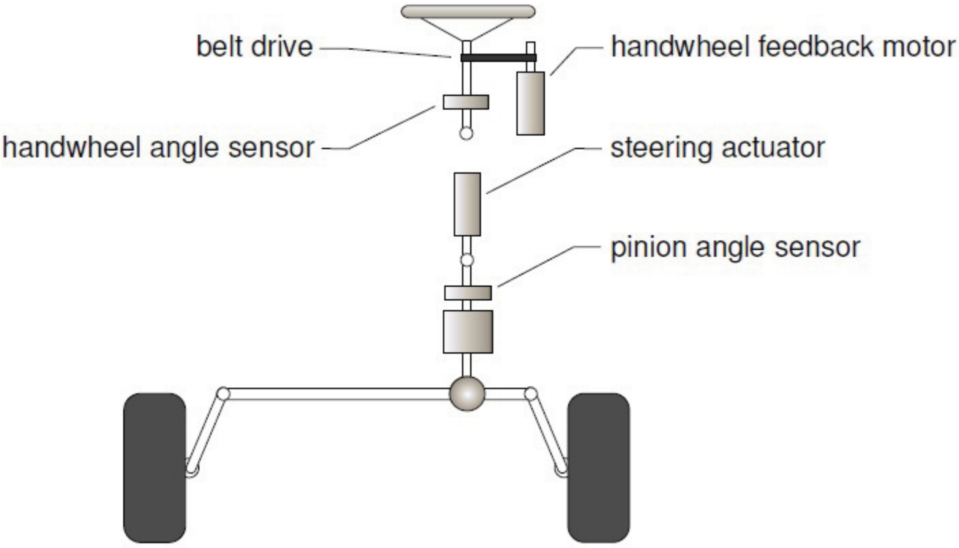

Fig. 1.5 Steer-by-wire configuration (Yih and Gerdes, 2004)

In the layout shown in Fig. 1.5, there is no steel rod to transmit the steering command from the steering wheel to the steering mechanism. Instead of that mechanical sub-system, there is an electronic system that measures the angle of the steering wheel by means of a sensor, processes the signal and actuates the steering mechanism with a motor. Also, a feedback system has been incorporated, using haptics. The feedback signal, mainly force feedback, is transmitted from the road to the steering mechanism through the front wheels, processing the feedback and using a second motor attached to the steering wheel to create the feedback torque. This torque is generally what a driver would feel if she or he were driving a standard automotive vehicle, except if the driver decides to alter the reconfigurable steering feedback.

This technology has several advantages and disadvantages. Its main benefit is the ability to adjust the steering behaviour of the automotive vehicle, and the corresponding feedback, with ease. In reality, any active algorithm to process the inputs given by the driver can be implemented and, by means of a stand-alone mechanical architecture, electronically controlled. The steering mechanism is no longer forced to always move proportionally to the steering angle. It may also react differently, depending on the system variables and parameters. An electronic system can, for example, detect a dangerous set of commands from the driver (such as trying to turn quickly at a high speed) and adjust the signal sent to the motor actuating the steering mechanism so that the final movement made by the vehicle is no longer dangerous. One can also, as an additional example, imagine a coefficient of proportionality that would adapt to the heading velocity of the vehicle, so if the vehicle is going fast the coefficient is low, to increase precision, and at low speed the coefficient would be high to increase maneuverability. The previous statements are just simple examples of the ability of the X-by-wire technology to modify the vehicle handling characteristics, as researched by Yih and Gerdes (2005). Active steering algorithms have been used to improve vehicle dynamics because “in continuous operation, active steering improves the roll dynamics” (Ackermann et al., 1999). As another example, the X-by-wire technology can be used for rollover prevention (Carlson and Gerdes, 2003). Moreover, because this kind of algorithm is simple to implement in a standard programming language such as C, an electronic system can readily implement it. Implementing such modifications using electronics is becoming a widespread trend (Leen, 2002). Besides, it has been shown that the feedback system gives good state estimation and improves the control of the vehicle as well (Amberkar, 2004; Laws, 2005). Other benefits are that the design of the mechanical system is made safer and easier by virtue of the disappearance of the steering column. Most of the electronic system can be made small and be placed anywhere in the vehicle.

Only a handful of recent automotive models use steer-by-wire technology, the main reason being reliability concerns. Many drivers feel that vehicles that are electronically controlled can never be reliable (Wilwert, 2005). Indeed, the benefit of a standard steering column is that the piece of steel will always transmit commands, if not damaged in crash. Extensive research has been carried out on X-by-wire reliability (Anwar, 2012; Oh et al., 2004; Yao, 2006; Yih, 2005; Zheng, 2005), especially on error treatment, and is still being researched to ensure that a safe electronic system can be implemented. This area of research includes control incorporating disturbance observers (Im et al., 2007). Contrary to what most customers believe, steer-by-wire actually even improves stability control responsibility (Hayama and Nishizaki, 2000), and yaw-rate control (Hosaka and Murakami, 2004). There has also been research carried out on optimization of X-by-wire control (Hac et al., 2006) and trajectory-tracking based on steer-by-wire (Setlur, 2002).

The steering-mechanism-by-wire is a different concept, substituting the steering mechanism (a four-bar linkage often plays that role in standard automotive vehicles) with its electronic equivalent. Although steer-by-wire is an electronic equivalent of the steering column, mechanical steering is still part of the process. One reason to not rely on a mechanical steering is related to the Ackermann principle, as explained in

Section 1.2.

1.1.4 Differential-by-wire

Differential-by-wire also plays a key role. When this method is implemented, angular velocities of the traction wheels are produced, not through a standard mechanical differential mechanism, but by means of a computer. Indeed, the outputs of this computer are transmitted to stand-alone motors actuating the traction wheels. Since this computer is capable of using any suitable control algorithm and sends commands to stand-alone motors, any two angular velocities can be produced.

1.1.5 Fly-by-wire

Fly-by-wire consists of X-by-wire applied to airplanes instead of automotive vehicles. Actually, fly-by-wire appeared prior to drive-by-wire, since a patent was published (Redmond, 1972) about 30 years before the first publication on steer-by-wire appeared. In fact, ways to export the ideas behind fly-by-wire from airplanes to automotive vehicles have been researched (Santon and Marsden, 1996); these publications are probably the reason for the development of X-by-wire. In modern aircraft fly-by-wire is the standard architecture, as opposed to the automotive industry, where an electronic architecture is not yet a mainstream technology. Fly-by-wire comprises chapters of books on standard avionics (Collinson, 2011).

1.2 Use of Ackermann Steering

1.2.1 Ackermann Approximation and Alternative Strategies

Of special relevance to standard automotive vehicles is the Ackermann steering (Mitchell et al., 2006), whose principles and derivations will be presented in section 2.1. As a matter of fact, standard mechanical steering mechanisms, including four-bar linkages, cannot satisfy the Ackermann conditions (Xiaoping and Jinming, 2003). Such equations are approximated only by means of the standard mechanical layouts. Due to wheel deformation, however, the Ackermann conditions needn't be exactly satisfied.

For purposes of improved dynamics at high speeds, a common and clever strategy consists in not satisfying the Ackermann conditions, by implementing alternative equations for the front wheel angles and rear traction angular velocities. Indeed, at high speeds and steering angles there are strong centrifugal forces. By resorting to field tests, the compensation of these inertial forces has been proven important for automotive vehicle manufacturers, in order to limit sliding and automotive crash.

Thus, of particular interest to the X-by-wire technology is any control program using Ackermann conditions at low speeds and other formulas at high speeds. Using an electronic system to implement such behaviours is a smart strategy, since these behaviours are programmable. Indeed, even if mechanical Ackermann steering could be created, it would be difficult, if not impossible, to produce different behaviours depending on the system variables. On the contrary, the behaviours of many electronic systems can be changed or reconfigured by means of standard programming. By the same token, beyond the steering system, this electronic paradigm is of interest in the design of all the other subsystems of an automotive vehicle. In particular, by implementing electronic equivalents of the differential mechanism and by attaching stand-alone motors to each wheel, any smart algorithm can be used to produce angular traction velocities.

1.3 Motivation

The objective of this thesis is to build a proof-of-concept complete X-by-wire prototype, test it and make conclusions about the benefits of such an architecture for automotive vehicles. Indeed, by-wire technologies are now well known, in particular steer-by-wire.

There has been a handful of automotive vehicles, including Mercedes-Benz and Nissan models, with steer-by-wire and brake-by-wire systems. Moreover, many prototypes using one or a combination of these by-wire technologies have been created and researched (Kelber and Webber, 2004; Pastorino, 2011).

Although they are well known, full X-by-wire architectures (using all or most of the by-wire technologies) have seldom been implemented, and never in commercial automotive vehicles. Furthermore, such prototypes are omni-directional (i.e., each wheel is steered and propelling the vehicle). Of these omni-directional complete X-by-wire prototypes, the first to combine all the by-wire technologies (Eder and Knoll, 2010) was built a couple of years before the beginning of the project described here. More recently, Xu (2014) published a book on a new omni-directional X-by-wire prototype.

The novelty of the work presented here lies in that the other prototypes have not been tested in the field; only in simulation. The main purpose of the work described in this thesis is, therefore, to create a complete X-by-wire prototype, rear-drive and front-wheel steering (so that our model closely resembles the more common architecture), and to prove that the new architecture can be implemented in automotive vehicles by testing it in the field.

1.4 A Project Within the APC Program

The project reported here, within the framework of the *Automotive Partnership Canada* (APC) Program, is an effort to make the fully electric automobile a reality. APC is a collective R&D program, a cooperation between five Canadian federal research and granting agencies, for the benefit of the entire Canadian automotive industry.

1.5 Scope and Organization of the Thesis

The rest of this document is organized as follows: Chapter 2 describes the process of mechanical and electronic design. Chapter 3 describes the tests that were implemented. Chapter 4 is a simple dynamic analysis of limit of grip and skidding behaviors of the prototype. Chapter 5 includes conclusions and recommendations for future work.

1.6 On Notation

In following the notation adopted by Springer's Handbook of Robotics (Siciliano and Khatib, 2008), scalars are represented with italics, vectors with lower-case bold faces, matrices with their upper-case counterparts.

Chapter 2

Mechatronic Design

In this chapter, the Ackermann principle and the corresponding equations are presented. They will be satisfied by an automotive robot, the design of which is presented in the later sections of this chapter.

2.1 Derivation of the Ackermann Equations

Crucial to our discussion is the concept of Ackermann steering. An Ackermann steering mechanism, be it mechanical or electronic, satisfies the Ackermann principle. This concept is best illustrated with the aid of a sketch, as shown in Fig 2.1. This figure shows a simplified top view of a rear-drive and front-steered automotive vehicle, with perfect Ackermann steering.

We label the automotive vehicle assemblies with numbers as indicated below:

1: Rear left wheel
2: Rear right wheel
3: Front right wheel
4: Front left wheel
5: Chassis

The parameters, inputs and outputs of an automotive vehicle are also shown in this figure. Concerning the parameters,

a is the wheelbase,
b is the track,
r_s is the scrub radius,
r_w is the diameter of the wheels.

We assume that the vehicle has four wheels of the same diameter. Regarding the inputs,

ϕ is the steering angle, given by the steering wheel,
v is the heading velocity, given via the pedals,

and the outputs

ϕ_1 is the angle of vertical rotation of the left front wheel,
ϕ_2 is the angle of vertical rotation of the right front wheel,
w_1 is the angular velocity of the left rear wheel, and
w_2 is the angular velocity of the right rear wheel.

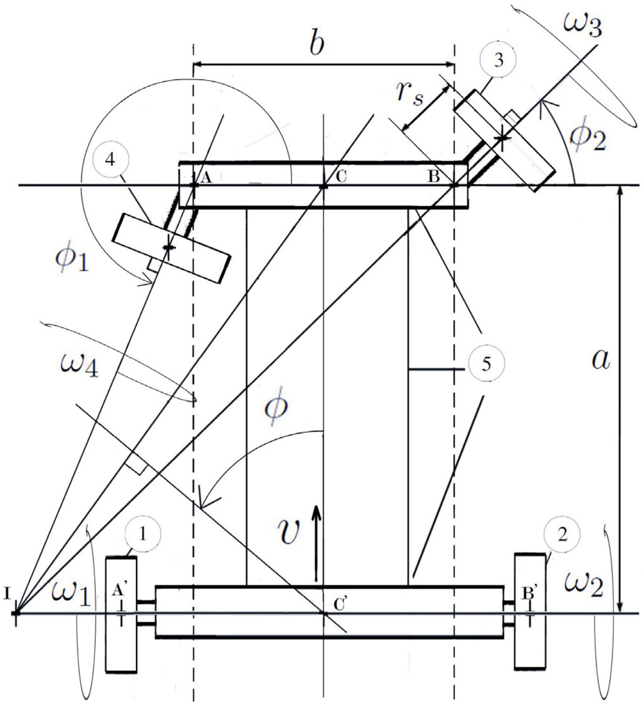

Fig. 2.1 Ackermann steering

The Ackermann conditions are explained in this Section by assuming that all moving bodies (mainly chassis and wheels) are rigid and move under pure rotation with respect to the ground. Under these conditions, the magnitude of the velocity of the centroid of each wheel is proportional to the distance to the common instant centre of rotation. Because all the wheels of the vehicle have, by assumption, the same diameter, the angular velocities of the wheels are also proportional to the distance to the common instant centre of rotation. The outputs are expressed below, in terms of the inputs and parameters of the vehicle, by using the Thales theorem and trigonometric substitutions. These relations were derived in the case of a strictly positive angle ϕ, when the vehicle is turning left. They also hold for $\phi = 0$ and $\phi < 0$, when the vehicle either travels on a straight course or, correspondingly, turns to the right. Furthermore, steering angles smaller than $-70°$, or greater than $70°$, are not considered here.

$$\phi_1 = \pi + \arctan \frac{\tan\phi}{1 - \dfrac{b\tan\phi}{2a}} \tag{2.1a}$$

$$\phi_2 = \arctan \frac{\tan\phi}{1 + \dfrac{b\tan\phi}{2a}} \tag{2.1b}$$

$$\omega_1 = \frac{v}{2\pi r_w}\left[1 - \frac{(b+2r_s)\tan\phi}{2a}\right] \tag{2.1c}$$

$$\omega_2 = \frac{v}{2\pi r_w}\left[1 + \frac{(b+2r_s)\tan\phi}{2a}\right] \tag{2.1d}$$

Since $\phi \in [-70, 70]$ in degrees, $\tan\phi \in [-2.8, 2.8]$, unbounded values of $\tan\phi$ never occur in the above relations. Furthermore, at the end of the detailed design, $b/2a = 0.258$. Hence $(b\tan\phi)/(2a) \in [-0.73, 0.73]$ and hence, $1 - (b\tan\phi)/(2a) \in [0.26, 1.73]$. Moreover $1 + (b\tan\phi)/(2a) \in [0.26, 1.73]$. The denominators in eqs (1.1) and (1.2) cannot thus vanish.

Moreover, by direct differentiation, expressions of the time-derivatives are derived:

$$\dot{\phi}_1 = \frac{\dot{\phi}}{1 - \dfrac{b\sin\phi\cos\phi}{2a} + \dfrac{b^2\sin\phi^2}{4a^2}} \tag{2.2a}$$

$$\dot{\phi}_2 = \frac{\dot{\phi}}{1 + \dfrac{b\sin\phi\cos\phi}{2a} + \dfrac{b^2\sin\phi^2}{4a^2}} \tag{2.2b}$$

$$\dot{\omega}_1 = \frac{\dot{v}}{2\pi r_w}\left[1 - \frac{(b+2r_s)\tan\phi}{2a}\right] - \frac{v(b+2r_s)(1+\tan\phi^2)\dot{\phi}}{4\pi a r_w} \tag{2.2c}$$

$$\dot{\omega}_2 = \frac{\dot{v}}{2\pi r_w}\left[1 + \frac{(b+2r_s)\tan\phi}{2a}\right] + \frac{v(b+2r_s)(1+\tan\phi^2)\dot{\phi}}{4\pi a r_w} \tag{2.2d}$$

Furthermore, for debugging purposes of the control system of the full X-by-wire proof-of-concept prototype, the following inverse Ackermann equations have been derived:

$$v = \pi r_w(\omega_1 + \omega_2) \tag{2.3a}$$

$$\phi = \arctan\left[\frac{\tan(\phi_1 - \pi)}{1 + \dfrac{b\tan(\phi_1 - \pi)}{2a}}\right] \tag{2.3b}$$

$$\phi = \arctan\left[\frac{\tan\phi_2}{1 - \dfrac{b\tan\phi_2}{2a}}\right] \tag{2.3c}$$

$$\phi = \arctan\left[\frac{2\pi r_w a}{b+2r_s}\,\frac{\omega_2 - \omega_1}{v}\right] \tag{2.3d}$$

Verification that $|\phi| \neq 0$ and hence, that there is no division by 0, is required. Through substitution of the maximum and minimum values of the steering angle in the Ackermann equations (1.1) and (1.2), $\phi_1-180\in[-60,85]$ in degrees and $\phi_2\in[-85,60]$ in degrees. Hence $\phi_1-\pi$ and ϕ_2 can never be equal to $\pi/2$. Moreover, $b/(2a)=0.258$, hence $1+(b\tan(\phi_1-\pi))/(2a)\in[0.55,3.96]$ and $1-(b\tan\phi_2)/(2a)\in[0.55,3.96]$, which means that there is no division by 0 in eqs(1.10) or (1.11). Furthermore, if the vehicle does not have wheels of the same diameter, as in tractors, the previous equations can be adapted and hold by introducing the different wheel diameters.

2.2 Mechanical Design

In this Section, the mechanical design of the prototype is described. We begin by explaining the functional requirements. Afterward, the final detailed design, including the mechanical and electronic subsystems, are discussed. For purposes of clarity and to explain the details of the mechanical design, the prototype is broken down into mechanical subsystems, namely the chassis, the suspensions, the front steering mechanism, the rear driving structure and the battery box. The rest of the prototype components are electronic hardware and will be presented in the second Section. Various mechanical engineering handbooks have been used during the design process (Avallone, 2007; Budynas and Nisbett, 2008; Chevalier, 2004; Oberg, 2008) together with a book on kinematics (Angeles, 1988).

2.2.1 Conceptual Design

Functional requirements and their Implementation

Of utmost importance are the functional requirements to understand the rationale behind a given design. The following Sections sum up the whole design process and the final layout, obtained at the end of the process. The process is described as if it had been purely sequential; in reality it consisted of many iterations. For example, to determine the dimensions of the chassis, an estimate of the maximum mass that could be placed on top of the suspensions was necessary, but at the same time, to determine the dimensions of the suspension, it was necessary to assess the weight of the chassis. A standard model of the design process is shown in Fig. 2.2.

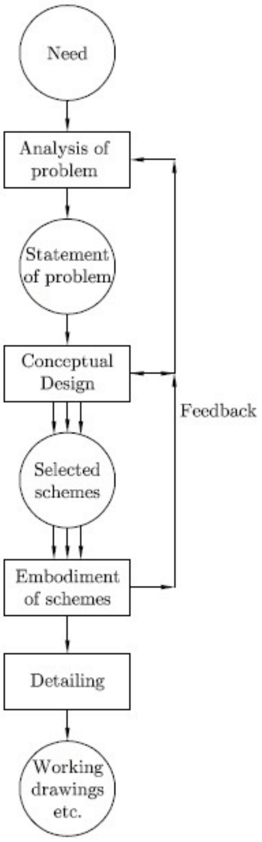

Fig. 2.2 French's Model (Angeles, 2011a)

The goal was to create a prototype mimicking as much as possible a chosen automotive vehicle, in order to prove that by building a small prototype to be tested in the field, this complete X-by-wire architecture could be implemented in automotive vehicles.

- The first and most important part of the design process, in order to mimic an existing automotive vehicle, is to create a layout with the same proportions as a particular model, so that after choosing it, the final proof-of-concept prototype behaves as this particular model. After carrying out a feasibility study and a short market survey, we have chosen the Toyota Tacoma, as explained in Section 2.1.2. The proportions of the track, wheelbase and diameter of the wheels have been selected as the relevant criteria. These parameters appear in the Ackermann equations; their values were readily found, as opposed to the value of the scrub radius, which was impossible to scale and therefore excluded from the scaling criteria.
- An important objective was to mimic the dynamics of the chosen model. Hence, the maximum speed (for the sake of brevity, in terms of maximum heading velocity), acceleration time and maximum slope

have been mimicked. The speed has been scaled down by means of simple division, which gives a maximum of 15 km/h or 4.17 m/s. These values, which have been found after a few design iterations, produce a scale of 3:20. The acceleration time is the same as that of the automotive vehicle, i.e., 7 s, which, in turn, leads to a maximum acceleration of 0.59 m/s^2, when we take into account the chosen maximum speed. A maximum slope has been chosen, equal to 20%, influencing the choice of traction motors.

- We assumed that the testing terrain would be horizontal. In fact, the prototype was to be tested at McGill and indoors, which, in turn, limits the size of the prototype. This means the prototype should occupy an area of 80×10^{-4}m^2, while having a length and width bigger than 30×10^{-2}m.
- Because of deadlines, funding and information constraints, and also because it would have been utterly complicated, it was decided not to mimic the dynamics with more complex considerations. In essence, this process would first require extensive theoretical understanding (the most elaborate automotive dynamic models are very complex) as well as advanced design and manufacturing of a realistic chassis. Such considerations were beyond the scope of this thesis.
- Thus, an analysis of the best criteria to mimic automotive vehicle suspensions was carried out. Because of tight deadlines, the suspension is limited to accommodate vertical motion. The suspension was designed simply as a spring in a one-tip-closed tube pushed by a rod. The natural frequency of the vehicle should be around 1 Hz, to lie within the range of frequencies of terrestrial vehicles. Furthermore, the proportions of the deformations (i.e., elongation) needed to be about the same as in a standard automotive vehicle. The elongation constraint requires springs and, later, after the final design, the frequency constraint also requires springs since these are the elements with the lowest stiffness values among off-the-shelf components.

2.2.2 Embodiment and Detailed Design

Overall Dimensions, Market Survey

The overall dimensions of the prototype were determined so that the dimensions specified were satisfied. First, the proportions of a particular SUV (Sport Utility Vehicle) and the 3:20 scale were determined, to produce wheel radius, wheel base and track targets (physical quantities defined in Fig. 2.1). Another McGill APC team had come to the conclusion (through a general automotive market survey) that the outcomes of the APC Program will be implemented in electric SUVs. Hence, to choose a suitable vehicle to mimic, a SUV market survey was carried out; the results are recorded in Table 2.1. The survey is broken down into three SUV categories: pick-ups, vans and 2-axle trucks.

Parameter 1	Fiat Strada long bed	TTTACF	TTTDC
Wheelbase m	2.70	3.24	3.57
Track m	1.30	1.55	1.60
ρ	2.1	2.09	2.23
GVWR T	1.9	2.22	2.47
Payload T	0.7	0.60	0.57
Curbweight T	1.2	1.62	1.90
Type of fuel	D	G,D	G,D
Data found on	caradisiac.com	toyota.com	toyota.com

Table 2.1 Pickup Truck Parameters

Pickup Truck Parameters

In Table 2.1

ρ	wheelbase/track
TTTAC	Toyota Tacoma truck access cab
TTTDC	Toyota Tacoma truck double cab
GVWR	Gross vehicle weight rating
G	gasoline, and
D	Diesel

The GVWR is an automotive vehicle maximum safe weight. Weight calculations include curb weight, additional equipment that has been added, the weight of cargo and the weight of passengers. Everything is considered to determine whether the GVWR has been exceeded[1]. The payload is the weight of occupants, equipment and cargo that a truck transports[1]. The values of these parameters in Vans are shown in Table 2.2.

Van Parameters

Parameter 1	Fiat Doblo cargo Maxi XL	Mercedes Vito	Mercedes Vario	Ford Series E
Wheelbase m	3.1	3.20	3.45	4.70
Track m	1.3	1.40	1.75	1.80
ρ	2.4	2.3	1.97	2.6
GVWR T	2.37	2.27	5.22	5.99
Payload T	1.00	0.87	1.35	2.54
Curbweight T	1.37	1.40	3.87	3.45
Type of fuel	G,D	G,D	G,D	G,D
Data found on	fiat.com	mercedes-benz.co.uk	mercedes-benz.co.uk	ford.com

Table 2.2 Van Parameters

---

[1] source: http://trucks.about.com/

Two-axle Trucks

Parameter 1	MTGM V.C1	MTGM V.C9	MTGM V.C11LKBL	DAF FACF65
Wheelbase m	3.5	5.5	6.7	7.3
Track m	1.8	1.8	1.8	1.92
ρ	1.9	3.0	3.7	3.8
GVWR T	12	12	12	18
Payload T	7.4	7.3	7.8	12.77
Curbweight T	4.6	4.7	4.2	5.23
Type of fuel	D	D	D	D
Found on	mantruckandbus.fr	mantruckandbus.fr	mantruckandbus.fr	daf.com

Table 2.3 Two-axle Truck Parameters

These vehicles are like heavy trucks, except that they have only two axles. In Table 2.3 “V.” stands for Version (Model), and “MTGM” for ManTGM 12.250.

Analysis of the previous survey and determination of the main dimensions of the prototype

The proportions of the Toyota TACOMA access cab, shown in Fig. 2.3, have been chosen as the benchmark for the proof-of-concept prototype.

Fig. 2.3 Toyota Tacoma

This vehicle has average SUV dimensions. We have all the useful values of the parameters of the

Tacoma, namely, the wheel radius, wheelbase and track.

The wheels were chosen first, thereby giving the scale of the prototype, since we know the value of the Tacoma wheel radius. Then, the dimensions of the chassis were adapted to the wheels or, equivalently, to the scale.

Indeed, we wanted reliable wheels, made of robust rubber. After considering the available off-the-shelf components and the embodiment design, suitable for flat brushless motors, we concluded that there was only one possible choice of wheels, namely the Colson Performa wheels, whose diameter is 5 inches. The choice of wheels, in turn, yielded the scale by simple division with the Tacoma wheel radius; the scale is 3/20 ($\simeq 1/6$). One Performa wheel is shown in Fig. 2.4.

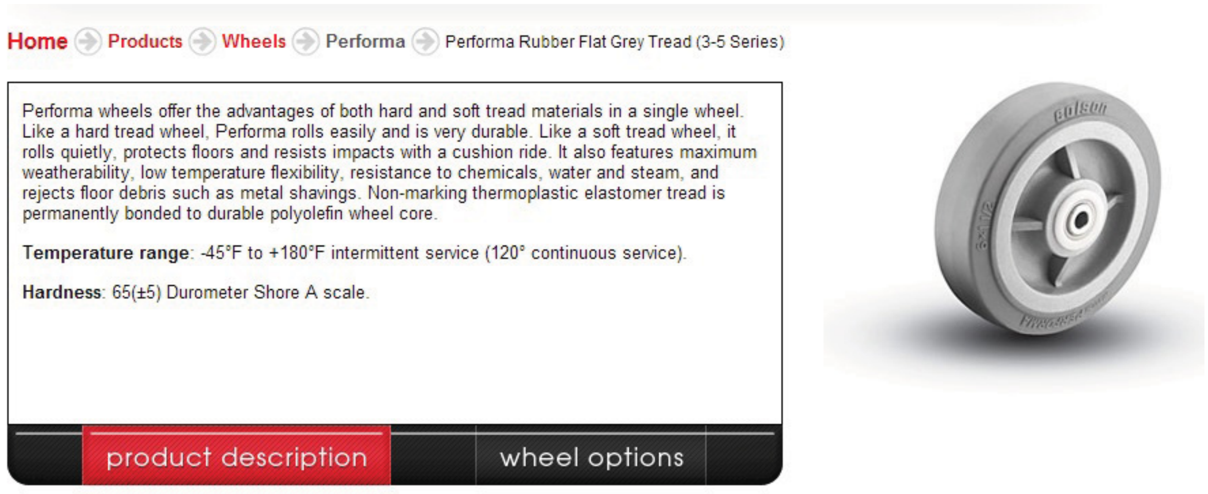

Performa wheels offer the advantages of both hard and soft tread materials in a single wheel. Like a hard tread wheel, Performa rolls easily and is very durable. Like a soft tread wheel, it rolls quietly, protects floors and resists impacts with a cushion ride. It also features maximum weatherability, low temperature flexibility, resistance to chemicals, water and steam, and rejects floor debris such as metal shavings. Non-marking thermoplastic elastomer tread is permanently bonded to durable polyolefin wheel core.

Temperature range: -45°F to +180°F intermittent service (120° continuous service).

Hardness: 65(±5) Durometer Shore A scale.

Fig. 2.4 Colson Performa wheels: http://www.colsoncaster.com/

These particular Colson wheels were chosen so that flat brushless motors of a diameter of 0.09 m (to be discussed in Subsection 2.2.3) can be attached directly to the wheels. Then, in accordance with the scale, the prototype had a wheelbase of 0.5m and a track of 0.24m. Once the dimensions were chosen, the rest of the detailed design could start.

Vibration Modelling and 1D Suspension

Given that the prototype was designed for tests on a flat, horizontal surface, the only criterion to decide on the stiffness of the suspension, in relation with the prototype mass, was the heaving frequency, which is known to be of the order of 1 Hz in all terrestrial vehicles, including passenger cars of all classes, trucks and even airplanes upon taxiing, taking-off and landing.

First, a simplified model of the prototype was derived so that we could have an idea of the heaving frequency we could reach and what it meant in terms of available mass. The model is standard and illustrated in Fig. 2.5. No dashpot is included, because there was no need for one in this study, as we were going to test the prototype on flat ground. For additional tests on bumps, we suggest to add proper damping systems, which were not implemented because of deadline constraints. The vibrational model used in this thesis consists of a mass on top of a spring.

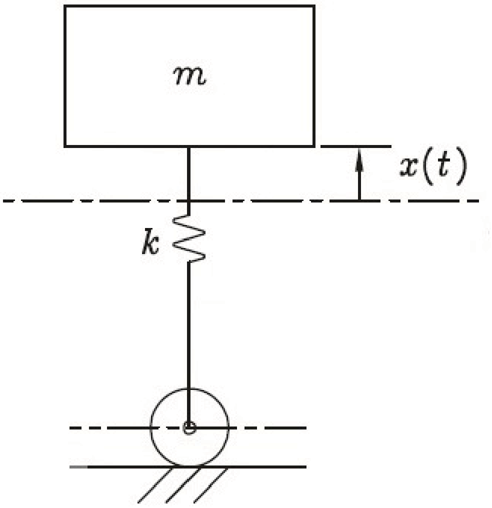

Fig. 2.5 Simplified dynamic model of the prototype (Angeles, 2011b)

The natural frequency of such a system is readily found as

$$f = \frac{1}{2\pi}\sqrt{\frac{k}{m}} \tag{2.4}$$

Where k is the equivalent stiffness constant of the four combined suspensions of the vehicle. Because four suspensions were placed in parallel in the final layout, the equivalent stiffness for the group of suspensions is

$$k = 4k_{\text{sus}} \tag{2.5}$$

Where k_{sus} is the stiffness constant of a suspension. Hence,

$$f = \frac{1}{\pi}\sqrt{\frac{k_{\text{sus}}}{m}} \tag{2.6}$$

After studying the available off-the-shelf components and trying to use four springs of the same model or combinations of different springs, we came to the conclusion that springs yielding a frequency equal to 1Hz are not available in the market. The frequency was much greater than 2Hz in the first layouts. Then we chose to place two springs of the same model in series inside a suspension, which led to

$$k_{\text{sus}} = \frac{k_{\text{spring}}}{2} \tag{2.7}$$

This solution was chosen because it divides by 2 the equivalent stiffness constant of one suspension, while keeping the same load-carrying capacity. Hence, it was applied to the spring whose physical quantities led to the smallest natural frequency of the prototype, when it was calculated for only one spring in every suspension. Using springs in series further lowers the heaving frequency; it yields a natural heaving frequency of 2Hz when using the spring whose characteristics are shown in Table 2.4. It was decided to keep this layout without adding another spring or several additional springs in every suspension. For proportions and stability considerations, this alternative strategy would have made the prototype too high, because of the resulting length of the suspension.

Type	Zinc-Plate Music Wire Closed and Ground Flat Ends
Stiffness Constant (lbs/inch)	5.50
Outside Diameter (inch)	0.24
Wire Diameter (inch)	0.029
Overall length (inch)	2
Compressed Length (inch)	0.69
Maximum Load (lbs)	7

Table 2.4 Characteristics of the spring chosen (http://www.mcmaster.com/)

After making several improvements to the suspension, we arrive at the final design, as shown in Fig. 2.6. A small steel rod pushes the two springs placed inside a Teflon tube (for reduced friction with the steel rod), while Teflon tube is inside a larger steel tube. There is a slotted spring pin going through the steel rod, a long slot cut in the bigger steel and the Teflon tubes. The pin is used to guide the translation of the rod into the tubes and to stop it at the two tips of the tube. Indeed a translation is desired, but not a rotation.

Furthermore, once the detailed design of the suspension was completed, the load-carrying capacity of the whole suspension is known. This capacity is equal to 12.7 kg, for the overall suspension.

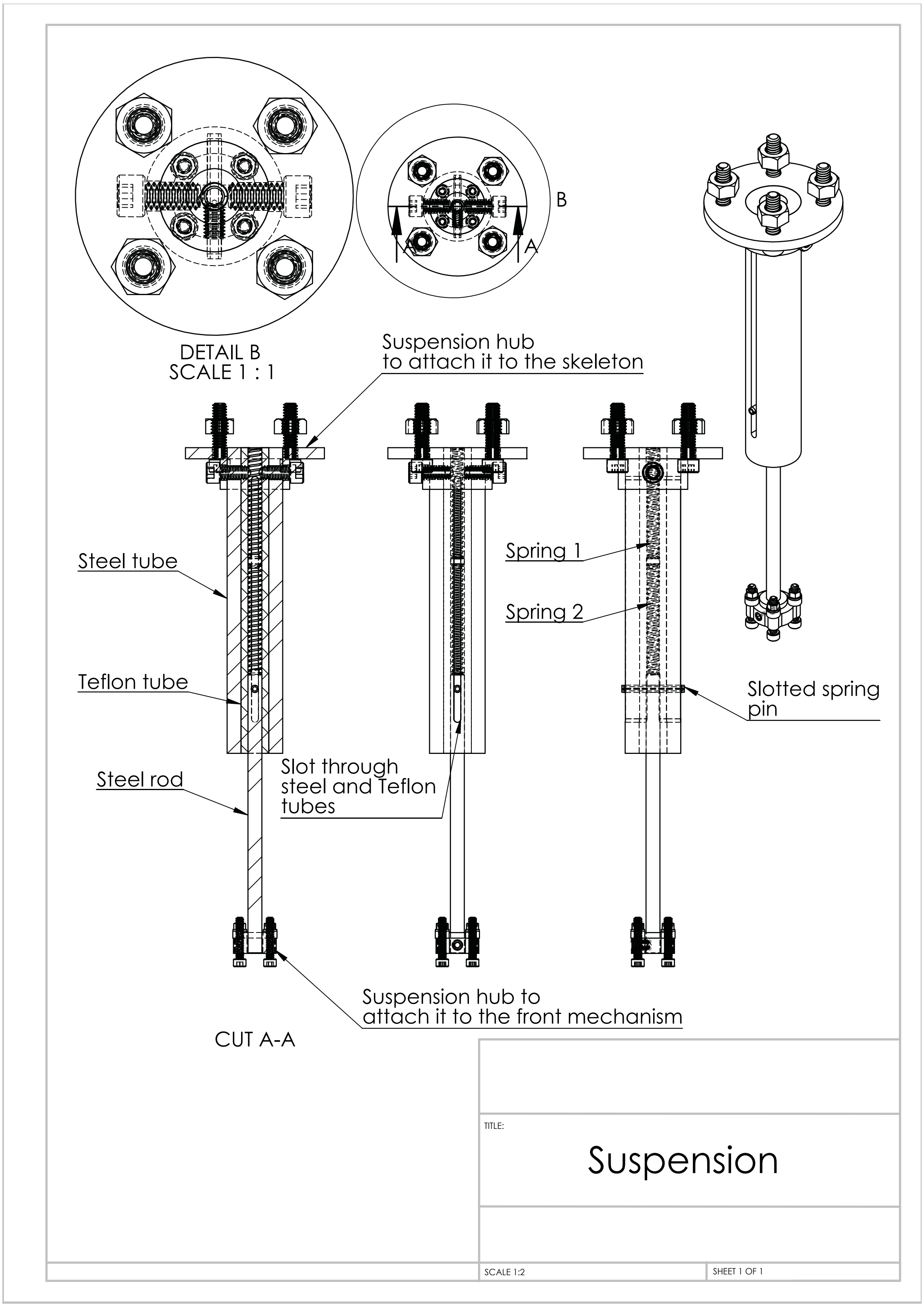

Fig. 2.6 Final suspension drawing

Detailed Design of the Chassis

First and foremost, in order to determine the maximum weight of the chassis, the elements that would be placed on top of the suspensions had to be listed. The larger steel tubes, Teflon tubes, chassis, Arduino cards, battery and its protection box were selected. In this context, steel for the chassis would have produced a structure that was too heavy and too large for our purposes; so it was thus decided to use 6061 Aluminum. That proved to be a good choice, as it allowed the prototype to have a strong (too large, on purpose) yet sufficiently light and easy to machine chassis, thereby not exceeding the load-carrying capacity of the springs within the suspensions.

The chassis is a bolted assembly of three U-channels (for assemblability purposes). The U shape is particularly robust during flexion. Furthermore, Fig. 2.7 below shows the load applied to the chassis, in a finite-element analysis conducted on Cosmosworks (the simulation module of Solidworks). This simulation consists of fixing the rear beam, on the left of the picture, and applying the weight of the battery and its box, as well as the reaction of the road. We modeled the weight of the battery, plus the box holding it, as a vertical downward force of 74.6N, since their mass is 7.6kg. Additionally, this weight was applied at the midpoint of the longest beam, since the box holding the battery would be attached to the main beam at this location. The reaction of the ground on the front wheels, which was to be transmitted to the chassis via the front suspensions, was modelled as a vertical upward force of 95.6N. This force corresponded to half of the total weight of the prototype, whose total mass is 19.5kg.

The maximum stress is 19 MPa, as shown in Fig. 2.8, and the highest stress is only observed in small regions, close to edges of the holes. Furthermore, the yield strength of Aluminum 6061 is about 240 MPa; hence the structure is sufficiently robust.

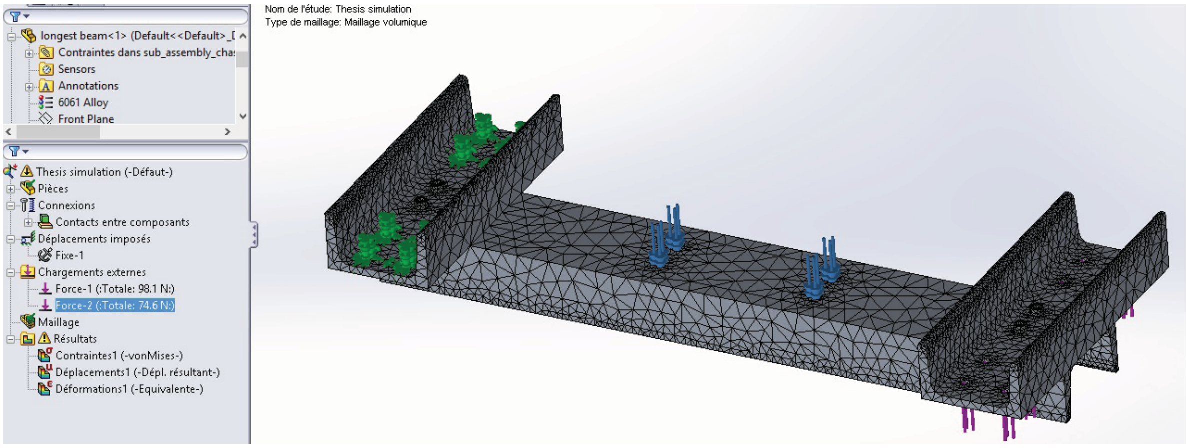

Nom de l'étude: Thesis simulation
Type de maillage: Maillage volumique

Fig. 2.7 Stress simulation: mesh and load

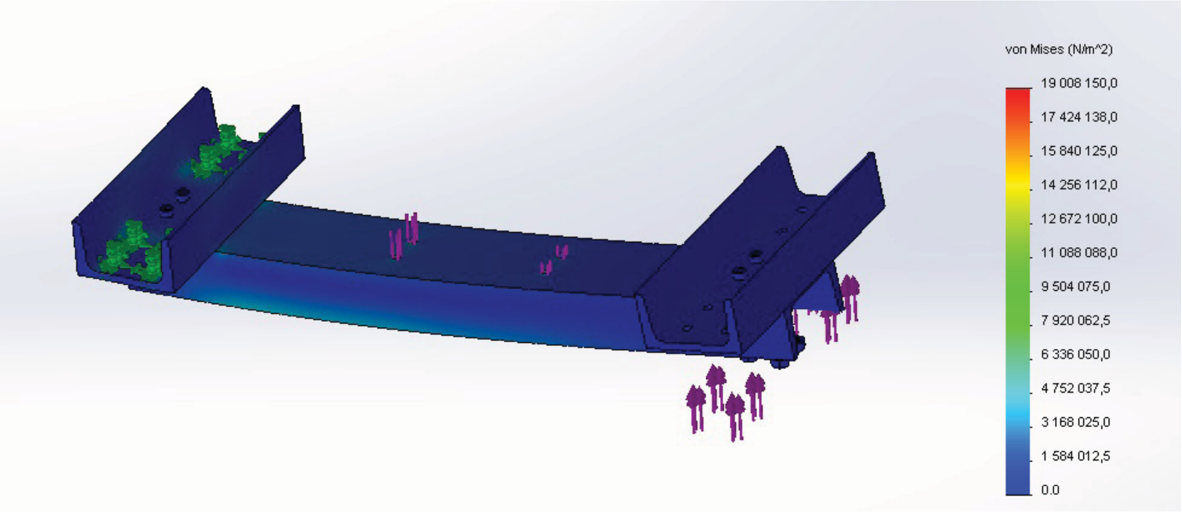

Fig. 2.8 Stress simulation: Von Mises stress results

Front Steering Mechanism

The front steering mechanism is placed under the two front suspensions. The front wheels are steered by means of two servomotors placed on top of two half-axles. The final design is shown in Fig. 2.9. The motor shafts, whose axes are pictured as vertical doted lines, are placed vertically and attached to the two plates that are, in turn, attached to four needle bearings. These bearings are connected to the two half-axles, which are mechanically independent.

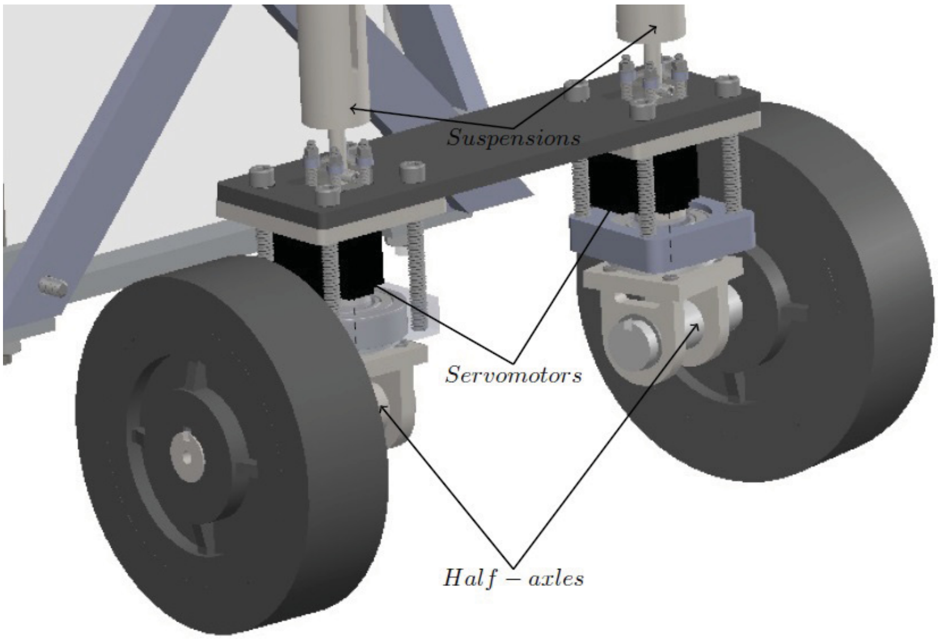

Fig. 2.9 Front steering mechanism

The front structure comprises reinforcing cages, in which the servomotors were placed. Figure 2.9 shows that, between the black servomotor on the left and the half-axle below it, a bearing is visible in the transparent plate. This bearing is a tapered-roller bearing, McMaster-Carr 5709K15. Such bearings were chosen for their ability to sustain both radial and axial (compression) loads.

In the final layout of the steering system, shown in Fig. 2.9, these bearings are placed so that the outer ring is below the inner ring, in order to transmit the reaction of the road (which can be broken down into a vertical upwards force and a torque) from the front wheels to eight screws, by virtue of two plates (the thickest ones in the figure, where the left one is transparent). Six of the eight long screws are visible in the figure; these screws are then used to transmit the load to the gray plates placed above the servomotors. Hence, the servomotors are not damaged by the reaction of the road, caused by the weight of the prototype. Nevertheless, these motors can make the front wheels turn with respect to vertical axes of rotation, by applying torques along vertical axes.

Rear Driving Structure

The prototype is by assumption a rear-drive vehicle. Although they propel the vehicle, the rear wheels must not turn about a vertical axis with respect to the chassis. Hence, the rear part contains the traction motors. This subsystem is also placed below the two rear suspensions. Its final design is shown in Fig. 2.10.

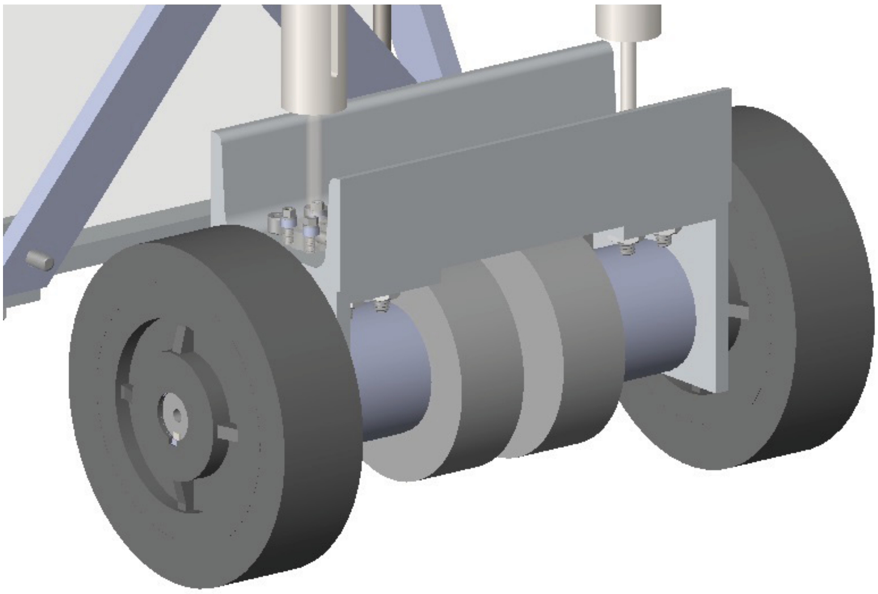

Fig. 2.10 Rear propelling structure

There is a short aluminum U channel, and to this channel are attached two brackets to mount the motor assemblies. The two larger and thinner cylinders are the two motors (cylinders that incorporate the two encoders), and the smaller cylinders (in terms of diameter) are the gear heads, attached to the output shafts of the motors. There is also one large hole in each bracket so that the shaft can go through it and be attached, by means of a shaft adapter, to the rear wheels. The dimensioning process and selection of the motors are explained in Subsection 2.2.4. Furthermore, the control cards of the motors and the plugs of the brushless motors are protected, by placing a square U bolt so that these electronic components will not be damaged, as, for example, when hitting the wall from behind. This square U bolt is shown in Fig. 2.11.

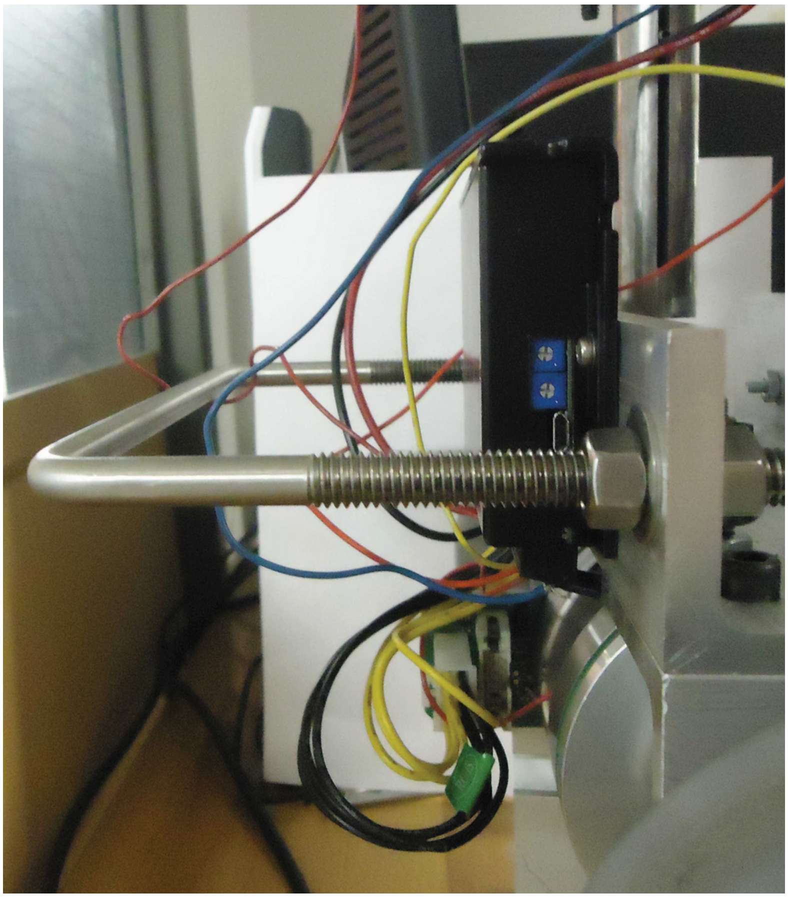

Fig. 2.11 Square U bolt used to protect a black control card and a motor plug

Box Containing the Main Battery

The box holding and protecting the battery was attached to the main beam of the chassis so that the weight of the battery would be considered on top of the springs with respect to the vibrational model and at the same time physically low to increase the stability of the prototype. This box, or cradle, is shown in Fig. 2.12. It comprises Aluminum narrow bars on top to attach the box to the longest beam of the chassis, several aluminum trusses to increase torsion and flexion stiffness as well as provide protection and a plate below the battery. The white box inside the trusses is the prototype main battery.

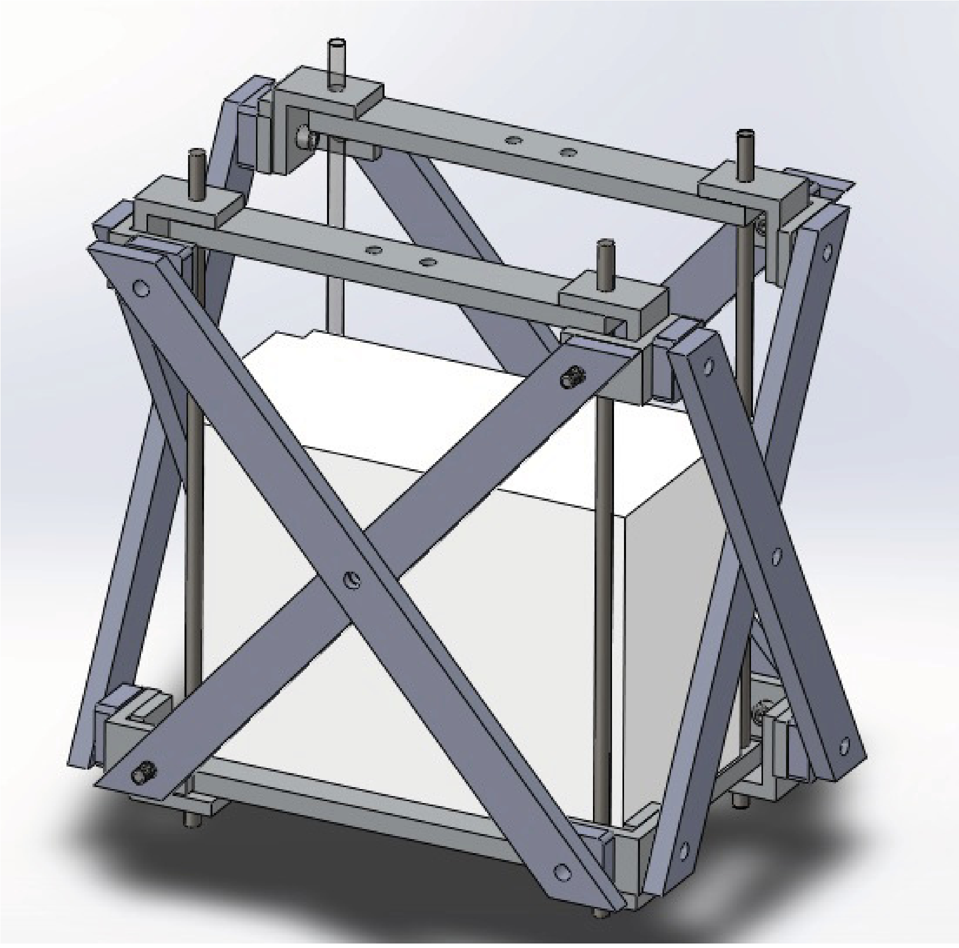

Fig. 2.12 Box holding and protecting the main battery of the prototype

2.3 Electronic Design

In this Section we present the electronic subsystems that controls the motors.

2.3.1 Overall Architecture

A steering wheel and pedals, connected to a laptop, are used to produce the steering angle, the heading velocity and button signals. These signals are controlled by software, and the outputs of the Ackermann equations (or the outputs of whatever algorithm the operator implements) are sent to the prototype. The signals arrive at an embedded computer (or to an electronic card) which transmits them to the motors. There is also a feedback system using the front wheel angles and the rear motor angular velocities, in order to transmit the signals to the control laptop. Figure 2.13 shows the first conceptual design that was drawn up.

The steering wheel and pedals kit are shown in Fig. 2.14, the Logitech Formula GP. In this diagram, four yellow buttons are shown, in between and close to the two large yellow shapes. The button on top and on the left is harder to see, but the steering wheel is symmetric with respect to a vertical plane. These four buttons are used to implement safety or choice features. For example, during the tests discussed in Chapter 3, the operator needs to press a particular button; otherwise the prototype stops immediately. There is another button that is used to switch between manual and programmed controls.

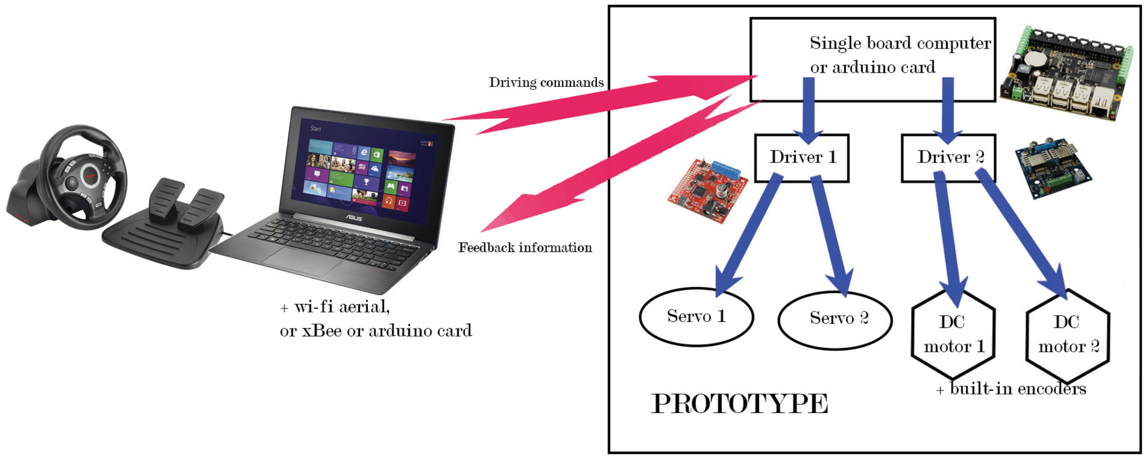

Fig. 2.13 Electronic conceptual layout

Fig. 2.14 Logitech Formula GP steering wheel and pedals

2.3.2 LabVIEW Program

LabVIEW (Laboratory Virtual Instrument Engineering Workbench) was chosen to create the control program, because it is a graphically-based programming language developed by National Instruments. Its graphical nature makes it ideal for test and measurement (TM), automation, instrument control, data-acquisition and data-analysis application (Margolis, 2012). Matlab Simulink was originally used, but we switched to LabVIEW when we started to work on data-acquisition.

The highest-level view of the architecture of the control system is shown in Fig. 2.15. The left side of the LabVIEW visual code corresponds to the steering wheel and pedals data reception as well as the feedback data from the Vicon system, to be introduced in Chapter 3. Inside the main rectangle, which is an infinite loop, the signals are processed, including safety filters. These filters include several error-treating systems. For example, if the signal sent to the VISA write box, that sends the numeric data to the Arduino board, is greater than 255, an algorithm makes it equal to 255. In fact, every piece of data sent to the Arduino board uses one byte. Hence, there cannot be any value greater than 255.

Furthermore, outputs of the Ackermann equations were computed and sent to the Arduino board on the right, outside the loop. The smaller rectangle loop, below the larger one, is another infinite loop in which the Vicon system feedback data are received, processed and displayed in graphs.

During the tests, the overall LabVIEW visual code is not what the operator sees. Instead, he or she sees the front panel, view shown in Fig. 2.16. This visual interface shows the inputs sent to the prototype ("v" and "phi" given through the pedals and the steering wheel), the feedback signals, the joystick information and the stop button to the LabVIEW control program. The graph on the left shows the feedback data received by the Arduino board. The two graphs on top show the prescribed values of the variables and the prescribed trajectory.

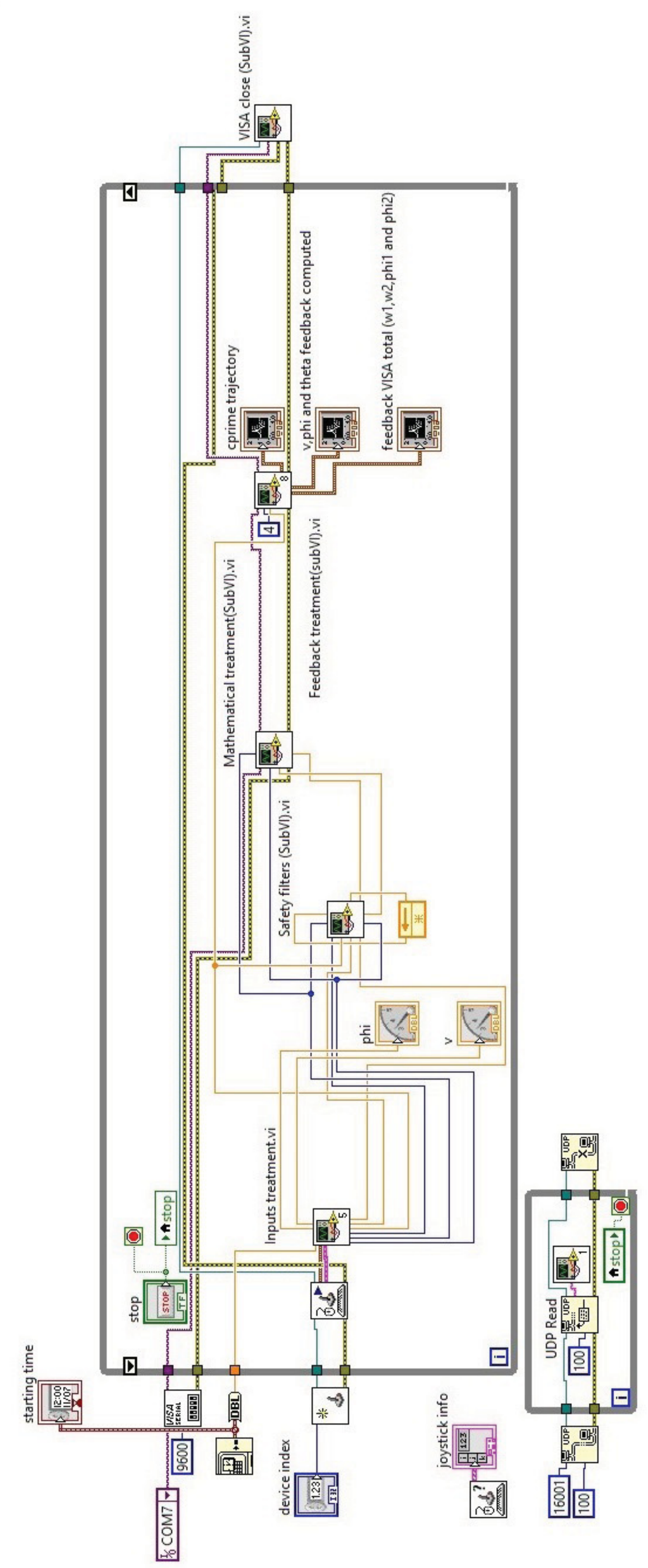

Fig. 2.15 High-level view of the LabVIEW control system

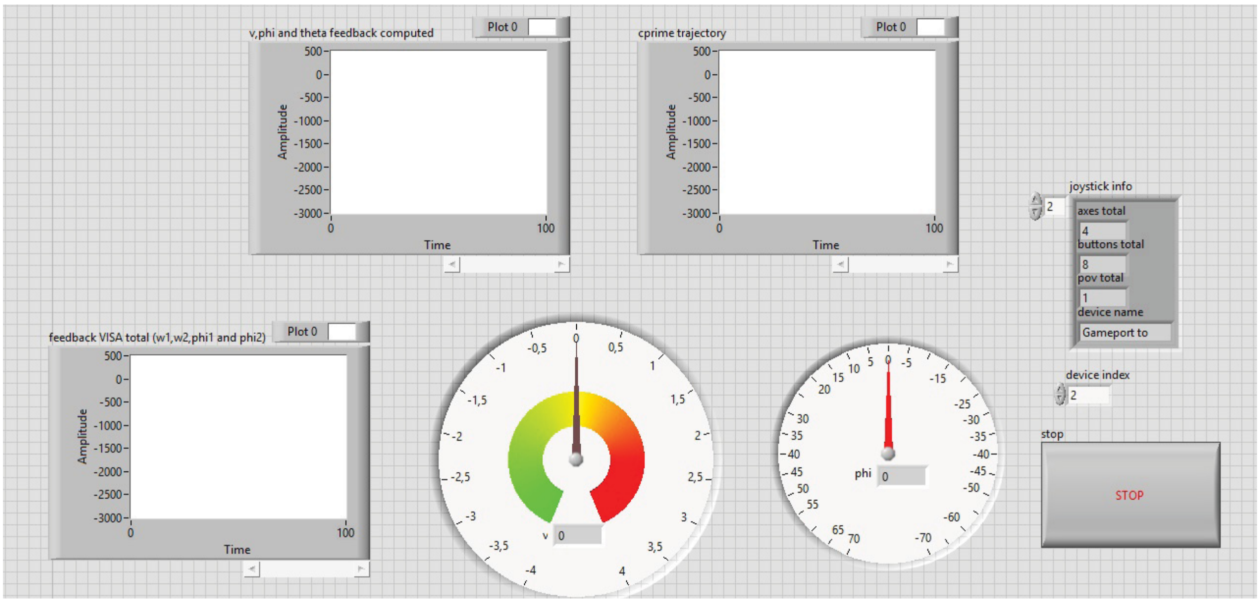

Fig. 2.16 User control interface of the LabVIEW control system

The LabVIEW code described here is complex, which means that difficulties arise when combining elements that are by themselves quite simple. One very important detail in the code is explained below. This detail is the direct computation of the Ackermann equations, seen in Fig. 2.17. Once the inputs ϕ and v have been filtered, on the left, and the automobile parameters are input to the program through constants, the program computes the outputs of the Ackermann equations.

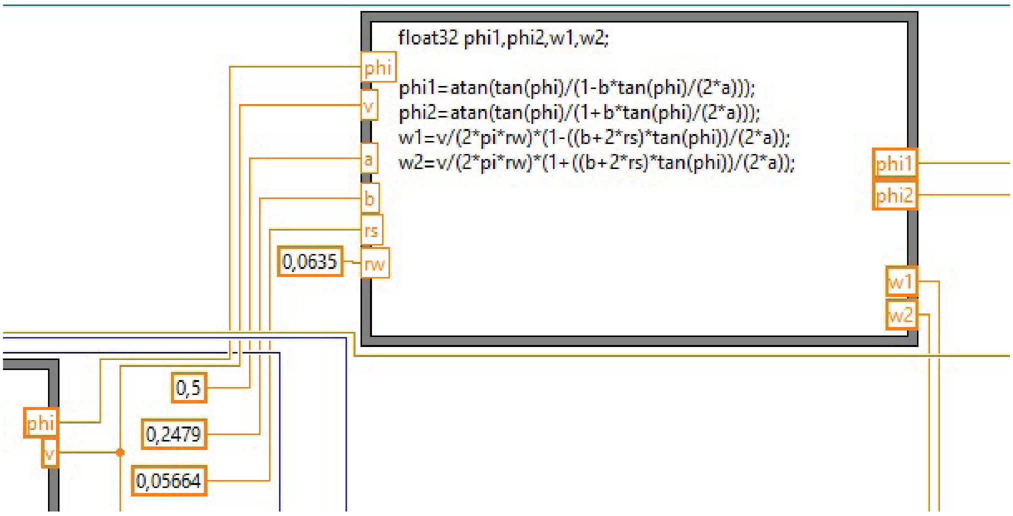

```
float32 phi1,phi2,w1,w2;

phi1=atan(tan(phi)/(1-b*tan(phi)/(2*a)));
phi2=atan(tan(phi)/(1+b*tan(phi)/(2*a)));
w1=v/(2*pi*rw)*(1-((b+2*rs)*tan(phi))/(2*a));
w2=v/(2*pi*rw)*(1+((b+2*rs)*tan(phi))/(2*a));
```

Fig. 2.17 Detail of the LabVIEW code: The computation of the Ackermann conditions

2.3.3 Arduino Implementation and Embedded Electronic Layout

Arduino technology was chosen as the embedded control system, since we can readily change or adjust the behaviour of an Arduino card by means of programming in a language similar to C. This technology does not require advanced knowledge of electronics. There are many tutorials and books (Bitter et al., 2007) that teach how to use it. Furthermore, taking into account calculation capabilities and complex technical factors we decided to use an Arduino Mega, shown in Fig. 2.18.

Arduino Detailed Capabilities and Control Program

The Arduino Mega 2560 is a microcontroller board based on the ATmega2560 (datasheet). It has 54 digital input/output pins (of which 15 can be used as PWM outputs), 16 analog inputs, 4 UARTs (hardware serial ports), a 16-MHz crystal oscillator, a USB connection, a power jack, an ICSP header, and a reset button[2]. A summary of the Arduino capabilities is shown in Table 2.5, the Arduino code is shown in the Appendix.

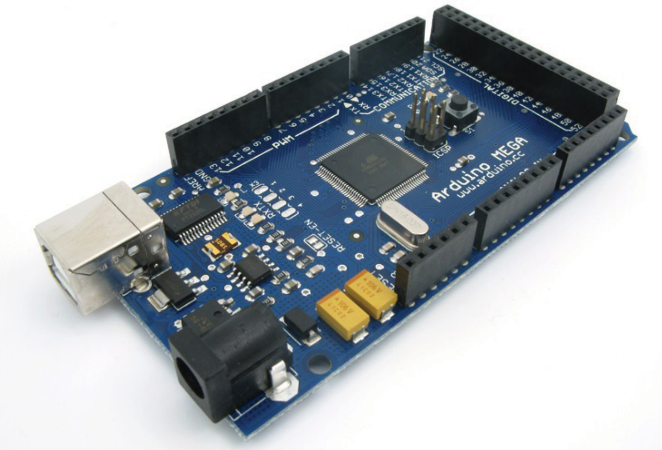

Fig. 2.18 Arduino Mega Card

---

[2] source: www.arduino.cc

Micro-controller	ATmega2560
Operating voltage	5V
Input voltage(recommended)	7-12V
Digital I/O pins	54 (including 15 PWM)
Analog input pins	16
DC current per I/O pin	0.040 A
Flash memory	256k with 8k for the bootloader
SRAM	8 kb
EEPROM	4 kb
Clock frequency	16 MHz

Table 2.5 Arduino Mega Technical Characteristics (arduino.cc)

Assigning Dimensions and Final Motor Selection

The Arduino card is connected to the two front servomotors, and to the two control cards of the rear brushless motors. First and foremost, we considered the traction motors, by means of a straightforward dynamic analysis of an automotive vehicle on a slope, as shown in Fig. 2.19, where

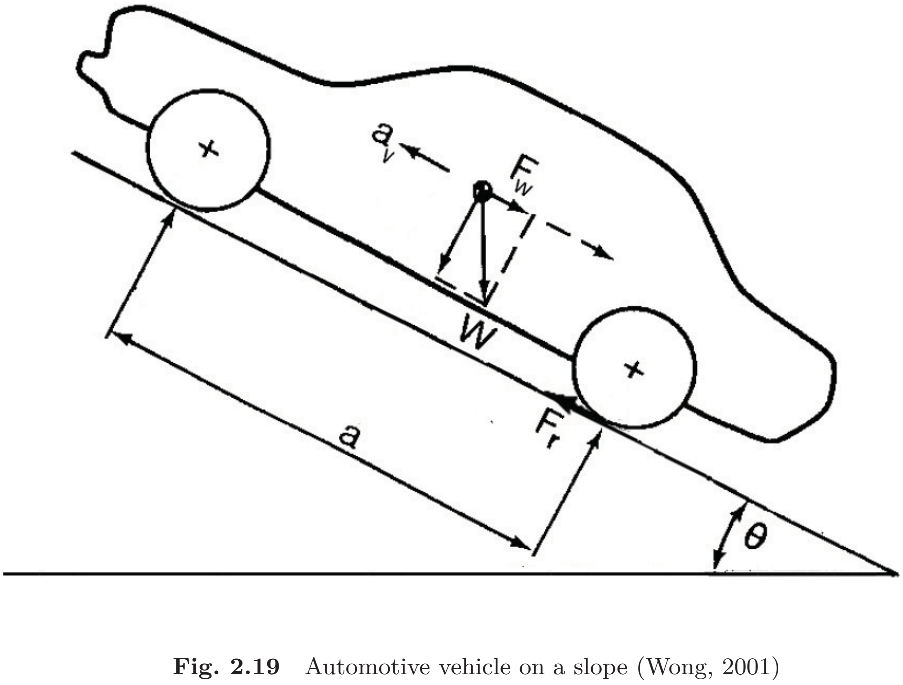

Fig. 2.19 Automotive vehicle on a slope (Wong, 2001)

F_r is the norm of the resulting traction force of the rear wheels,
W is the norm of the weight of the vehicle,
F_W is the norm of the projection of the weight along the direction of the traction force,
a_v is the norm of the maximum acceleration of the centre of gravity,
θ is the maximum slope,
a is the wheelbase, and
m is the total mass of the vehicle.

Newton Second Law yields

$$ma_w = F_R - F_W \tag{2.8}$$

with,

$$F_R = 2\frac{\tau_t}{r_w} \tag{2.9a}$$

$$F_W = mg\sin(\theta) \tag{2.9b}$$

and
g : the gravity constant,
r_w : the radius of the wheels and
τ_t : the maximum torque applied to a traction wheel, at the output shaft of a gear head, by a rear traction motor.

Hence, to be able to accelerate at maximum acceleration and on a slope corresponding to the maximum inclination, the condition below must be satisfied

$$\tau_t \geq \frac{mr_w(a_v + g\sin(\theta))}{2} \tag{2.10}$$

The condition below is used to select the steering motors. The worst-case scenario is a front wheel that is stuck in place, unable to rotate with respect to its half-axle. In that case, the wheel would need to slip on the floor, without rolling, while one-fourth of the total mass is supported by it. Then we take into account the friction coefficient between rubber wheel and dry concrete floor it slips on, called μ and equal to 0.85. The steering torque τ_s required would be equal to one-fourth of the total mass m of the prototype times the lever arm, the latter being equal to the scrub radius r_s. Hence,

$$\tau_s \geq \frac{mr_s\mu}{4} \tag{2.11}$$

Verification of the Chosen Motors

At this point we verified that the motors, that were selected after we had completed the detailed mechanical design and that will be introduced below, would provide sufficient torque. The brushless motors produce a maximum continuous torque of 0.56Nm, as shown in Table 2.6, and are attached to GP52C gear heads, whose gear ratio is 4.3, as shown in Table 2.7. They also have a maximum efficiency of 0.91, which is usually at its greatest while producing the said maximum torque. Furthermore, we assumed that the encoder did not alter the produced torque in any way. Hence, we arrived at the following expression of the resulting torque applied to a rear wheel:

$$\tau_t = \tau_{1rm} r_{gh} \eta_{gh} \tag{2.12}$$

where,

τ_t : the maximum torque applied to a rear wheel,

τ_{1rm} : the maximum continuous torque produced by a rear motor,

r_{gh} : the speed ratio of the gear heads, and

η_{gh} : the efficiency of the gear heads

At the end of the project, the mass of the prototype was found to be 19.5kg. By plugging the final values into the second term of equation (2.10) and into (2.12), inequality (2.10) is satisfied, i.e.,

$$\tau_t = 2.19Nm \geq 1.32Nm = \frac{mr_w(\mathbf{a_v} + \mathbf{g}\sin(\theta))}{2}, \tag{2.13}$$

which means that the traction motors provide sufficient torque to satisfy the requirements.

With regards to the front motors, the servomotors we selected were the Herkulex DRS0101, as shown below, whose stall torque is 1.18Nm, called τ_s. Since, at the end of the detailed design, r_s, the scrub radius, was equal to 0.05664m, eq (2.11) is satisfied, namely,

$$\tau_s = 1.18Nm \geq 0.23Nm = \frac{mr_s\mu}{4} \tag{2.14}$$

which means that the steering motors provide sufficient torque to turn the front wheels.

The Herkulex DRS0101 Smart Servomotors

In Fig. 2.20 two models of smart servomotors by DONGBU are shown. In this diagram, the servomotor on the left, the DRS0101, was chosen as the steering motors of the prototype. A diagram of the DRS0101 is shown in Fig. 2.21.

Fig. 2.20 Dongbu Herkulex DRS-0101 and DRS-0201 (Herkulex manual)

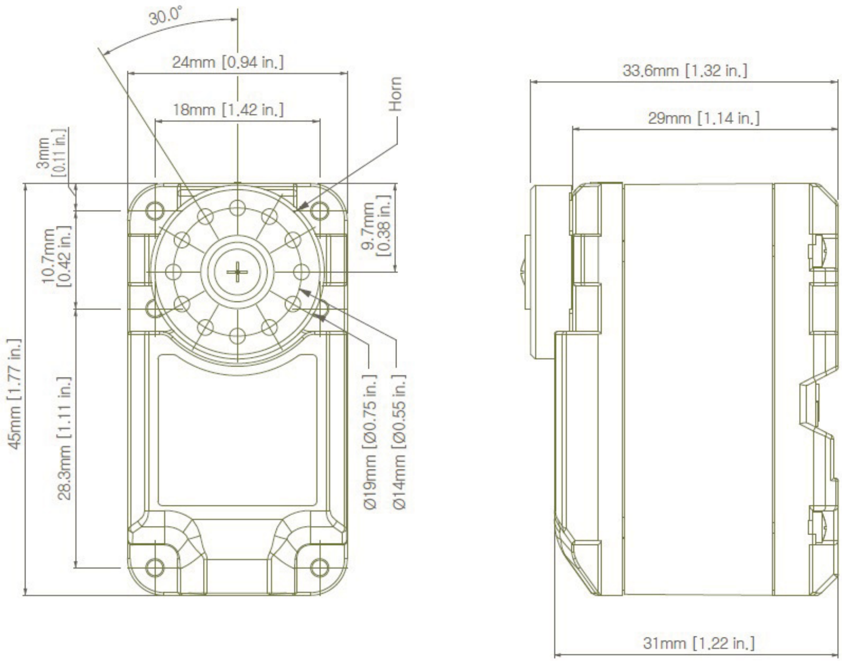

Fig. 2.21 Herkulex DRS-0101 drawing (Herkulex manual)

Of the utmost importance was the ability to control the servomotors with the Arduino board. This model of motor was selected because Arduino libraries already exist to control the Herkulex models in particular, thus allowing us to produce a much simpler code. For example, there is the command Herkulex.moveOneAngle(int servoID, float angle, int pTime, int iLed). This particular syntax commands one servomotor, whose ID number is "servoID", to turn by a given value "angle". The steering motors incorporate gear reducers and control systems capable of controlling the angle precisely, with a 0.325 degree resolution, while suppressing vibrations. Furthermore, they are also small and produce a high torque compared to the other servomotors of their class.

The servomotors need a 7.2V power supply, which cannot be provided directly by either the Arduino board or by the main battery, presented in Subection 2.2.4. Hence, for the sake of simplicity, a small 7.2V NiMH battery, with a capacity of 3 Ah was attached to the chassis of the prototype, stored inside the longest beam.

The Maxon EC90 Brushless Motors and Their ESCON 50/5 Control Cards

Part number	429271
Power(W)	90
Type	Brushless
Series	Flat
Overall diameter (m)	0.09
Max. permissible speed (rpm)	5000
Nominal speed (rpm)	2510
Max efficiency	0.87
Weight (kg)	0.6
Max. efficiency	0.91
Nominal voltage (V)	36V
Weight (kg)	0.460

Table 2.6 Maxon EC90 Flat Data (EC90 datasheet)

The EC90 motors can be purchased with gear heads attached to them. A representative gear head carries the technical characteristics shown in Table 2.7.

Fig. 2.22 Maxon GP52C Gear Head

The ESCON 50/5 control cards have various control capabilities, including speed control by means of an encoder or hall sensors built in the motor. The two cards, one per motor, receive data from the Arduino board, namely the absolute values of the targeted angular velocities, by means of two of their

Part number	223081
Gear head type	Planetary, spur gears
Output shaft material	Stainless steel
Speed ratio	4.3
Number of stages	1
Max. continuous torque (Nm)	4
Max. efficiency	0.91
Weight (kg)	0.460
Gear head length (m)	0.049
Maximum input speed (rpm)	6000

Table 2.7 Gear Head Data (Maxon GP52C datasheet)

analog inputs. Indeed, the Arduino board sends PWM (Pulse-Width Modulation) signals, which is a way to digitally generate an analog-like signal. Capacitors connected to the analog inputs of a control card, in turn, calculate the mean value of the voltage of a PWM signal, which is linearly mapped into a speed by the card. For example, 0-5V is mapped into 0-maximum angular velocity. Furthermore, two digital input pins of a control card receive a binary value, corresponding to a cw or ccw turn. Thus, the prototype can move forward of backward.

Finally, this card model has analog outputs that send the angular velocity feedback data to the Arduino board, whose noise is filtered by means of capacitors (low-pass filters). Hence, the Arduino board and the LabVIEW control program have access to the motor feedback data, but these data cannot be used to obtain the position of the prototype in an inertial frame. There is no information about sliding. Hence, the system is considered overall open loop, even though all the motors, rear or front, incorporate closed control loops, and these loops are only local.

2.3.4 Main Battery and Safety

The ESCON 50/5 control card, described in Subsection 2.2.4, has a nominal operating voltage between 10 and 50 VDC. Engineers from Electromate, a corporation working with Maxon, suggested the chosen combination of brushless motors, encoders, gear heads and battery. Their advice was to use a 48 V power supply with the ESCON 50/5 control card, to fulfill the needs of the prototype at maximum slope and acceleration. A Lithium-Ion battery was chosen to provide the energy required by the traction motors. Lithium-Ion batteries are very popular for small prototypes, since amongst standard batteries, the Lithium-Ion kind has the highest energy density. Characteristics of various standard kinds of batteries are shown in Fig. 2.23. Furthermore, the model chosen is a $LiFePO_4$ battery, since the $LiFePO_4$ is the safest of all Lithium-Ion batteries.

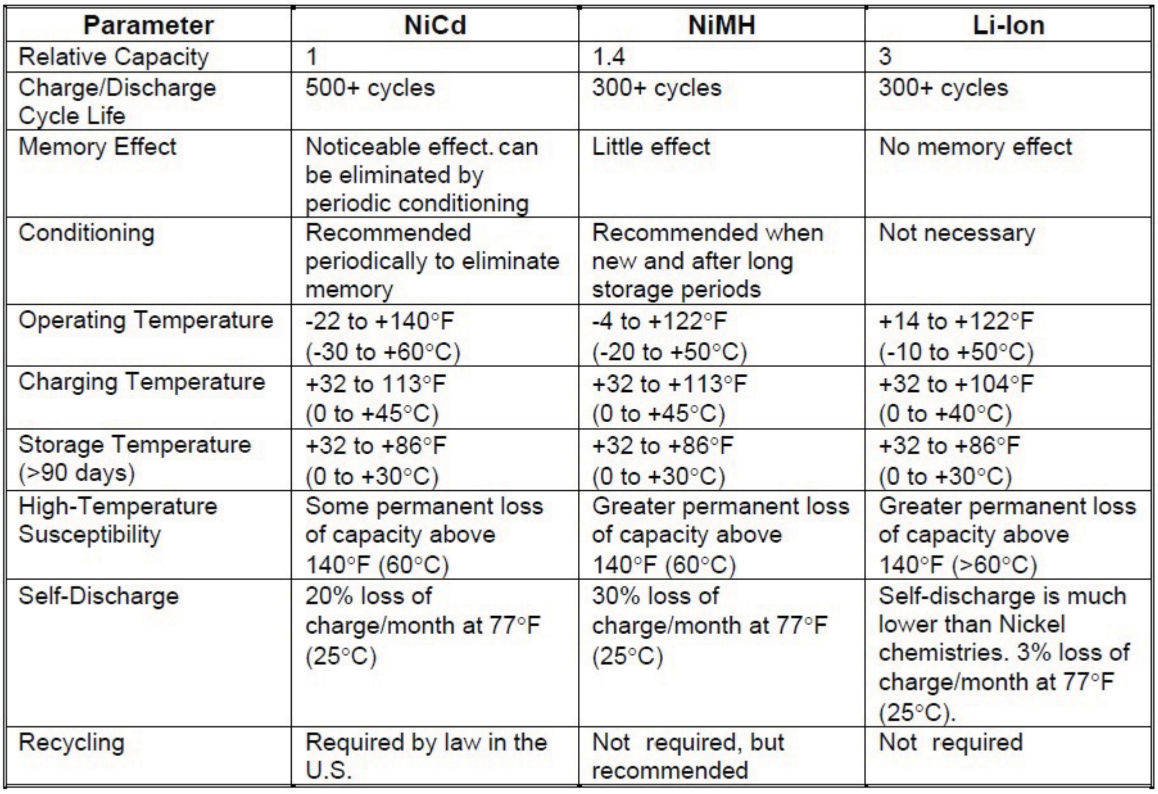

Parameter	NiCd	NiMH	Li-Ion
Relative Capacity	1	1.4	3
Charge/Discharge Cycle Life	500+ cycles	300+ cycles	300+ cycles
Memory Effect	Noticeable effect. can be eliminated by periodic conditioning	Little effect	No memory effect
Conditioning	Recommended periodically to eliminate memory	Recommended when new and after long storage periods	Not necessary
Operating Temperature	-22 to +140°F (-30 to +60°C)	-4 to +122°F (-20 to +50°C)	+14 to +122°F (-10 to +50°C)
Charging Temperature	+32 to 113°F (0 to +45°C)	+32 to +113°F (0 to +45°C)	+32 to +104°F (0 to +40°C)
Storage Temperature (>90 days)	+32 to +86°F (0 to +30°C)	+32 to +86°F (0 to +30°C)	+32 to +86°F (0 to +30°C)
High-Temperature Susceptibility	Some permanent loss of capacity above 140°F (60°C)	Greater permanent loss of capacity above 140°F (60°C)	Greater permanent loss of capacity above 140°F (>60°C)
Self-Discharge	20% loss of charge/month at 77°F (25°C)	30% loss of charge/month at 77°F (25°C)	Self-discharge is much lower than Nickel chemistries. 3% loss of charge/month at 77°F (25°C).
Recycling	Required by law in the U.S.	Not required, but recommended	Not required

Fig. 2.23 Comparison of different standard battery types
(by Tyco Electronics on www.portal.state.pa.us)

The relative capacity is the electrical capacity when compared to a NiCd pack.

The battery chosen was ordered from one of the few suppliers that could provide it, namely, PingBattery, in China. In fact, there were only a handful of choices for 48V $LiFePO_4$ batteries.

The main battery has a capacity of 10 Ah, its weight is 4.9 kg, and its dimensions are $0.200 \times 0.105 \times 0.150$ m. Since the chosen motors use a maximum of 10 A in combination, the battery lasts at least one hour from time of full charge. Such a powerful battery may be dangerous; a short circuit might burn other components or the battery itself. Hence, safety was given due attention. The electric equipment implemented to ensure safety comprise a terminal block and a panel-mount equipment circuit breaker. A terminal block was used to make sure that the output wires of the battery would never be in contact with each other. In addition, a general ON/OFF switch, which also incorporates a circuit breaker, was connected to the two batteries, the main battery for the traction motors and the smaller battery of the steering motors.

2.4 Overall View of the Assembled prototype

Figure 2.24 shows the final design, once it has been manufactured and assembled.

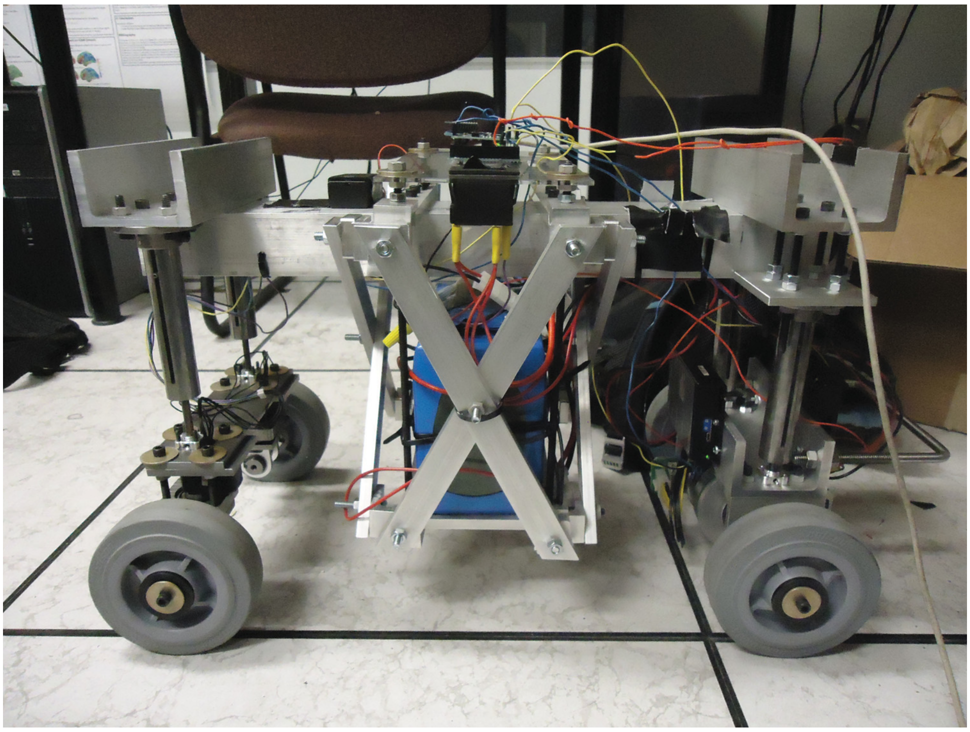

Fig. 2.24 Side view of the proof-of-concept prototype

Chapter 3

Tests and Analysis

This chapter includes an introduction to the Vicon motion-capture system, a presentation of the methodology used to test the proof-of-concept prototype, as well as the test results, and an analysis of these results.

3.1 Methodology Using the Vicon System

The Vicon system is a motion-capture technology that uses small balls as trackers; balls are attached to any physical object, and cameras are placed around the object, to obtain its pose in real time. Furthermore, during the measurements, one or several operators see in real-time a set of points in the shape of a polygon, each point being the location of a tracker, and a frame created with respect to these points, appearing on screens.

This system was chosen to test the robot because there were already several laboratories using it at McGill. Prior use is not the only advantage, however. The precision of this system is about 5 mm, which is far more precise than systems using GPS trackers. At the same time, this system is simple to set up, especially since there are already research team using it at McGill. In the particular setup used to test the X-by-wire robot, the system streams the data directly to the laptop running LabVIEW, via an Ethernet cable. Figure 3.1 shows the four Vicon trackers, which are balls encircled here, attached to the prototype, on top of its chatssis.

All the tests were performed in the same setting, at approximately the same starting point in the Aerospace Mechatronics laboratory, far from the origin of the default frame of the Vicon system. The starting point is of minor importance, provided that all the manoeuvres fit into a small virtual cube on the ground, where the Vicon system is capable of precisely measuring the positions of the four balls attached to the robot. The location and dimension of the said cube were measured. The cube is quite small, compared to the size of the laboratory, because the precision and measuring space of the Vicon systems increase with height. The X-by-wire of interest being a terrestrial vehicle, the measuring area was further limited and the precision was a bit lower, when compared to that of a flying robot, because this automotive robot is further away from the cameras. The Vicon setup is intended to track flying robots.

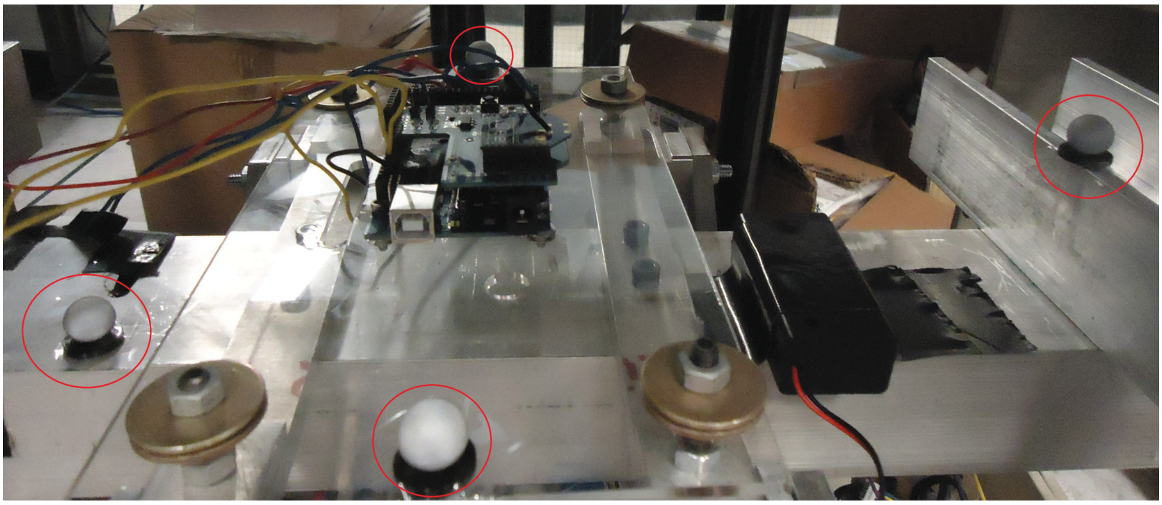

Fig. 3.1 The four Vicon ball trackers placed on the chassis

3.1.1 Description of the Tests

First, the proof-of-concept robot was to be tested while moving in a straight line. This test was used to prove that the control system is capable of following the simplest path. Afterward, the robot turned so that the influence of the heading velocity and steering angle on the error due to the drift was studied. Each measured turn, where there is slipping, is compared with the corresponding prescribed path that is satisfying the non-slippage assumption. Indeed, tests 2 to 4 are used to observe and quantify drift while the prototype is satisfying the Ackermann conditions. A description of the five tests that the robot underwent is shown in Table 3.1.

Test number	Heading velocity (m/s)	Steering angle (degrees)	Manoeuvre type
1	0.286	0	Straight line
2	0.226	–35	Turn
3	0.386	–35	Turn
4	0.462	–50	Turn

Table 3.1 Brief Description of the Tests

When examining every manoeuvre and when the data were acquired, we realized that the robot was never at the origin of the default frame; thus, new frames were created. A new frame is created by virtue of a pure translation so that the robot always starts to move at the origin of the new frame. Furthermore, for every manoeuvre, the robot is first roughly aligned with the first axis of the frame of the Vicon system, with the help of the real-time feedback this system provides. Once the robot is aligned with the X axis of the Vicon system, the test begins. Since this procedure is not precise, there was, on a few occasions, a small angle between the initial direction of the robot and the first axis of the frame. Hence, the data underwent a virtual rotation, to turn the trajectory to its proper orientation, which passes through the origin of the frame. A pure rotation of the trajectory is used to suppress any initial misalignment, and does not alter either the shape or the size of a trajectory.

3.2 Straight Line Manoeuvre

In Fig. 3.2 we show the results of the first test, representing the actual path of the robot versus its prescribed path. The latter is a segment. The length of this segment corresponds to the length of the largest arc among the next tests, namely 1200 mm.

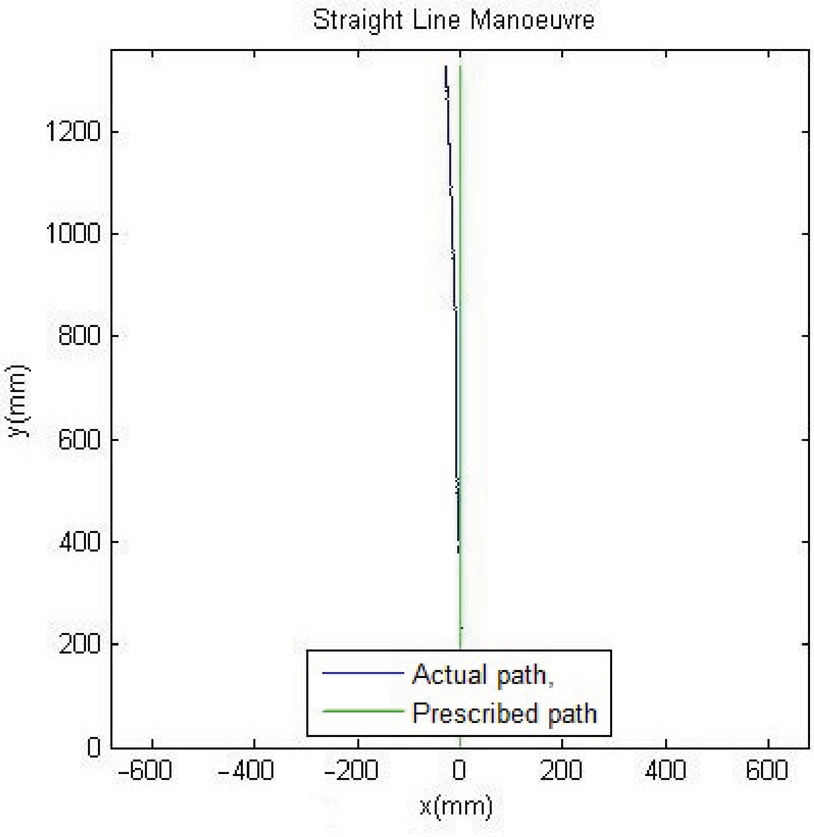

Fig. 3.2 Test 1

3.3 Turning Manoeuvres

Here we report on the results of the turning tests. Each prescribed path is a ninety-degree arc, whose radius depends only on the steering angle. We assumed pure rolling, which means no slippage. Of course, we expected some slippage during the tests, but the error was supposed to stay small, as the heading velocity and the steering angle were kept small, because of space and safety considerations. Furthermore, the radius of the prescribed path is expressed as

$$r = \frac{a}{\tan(\phi)} \tag{3.1}$$

where

r is the radius of the prescribed arc

a is the wheel base

ϕ is the steering angle

The wheel base and the steering angle are shown in Fig. 2.1. Tests 2 and 3, shown in Fig. 3.3, correspond to two turns at the same steering angle, −35°. The difference is that test 3 was carried out at a higher heading velocity.

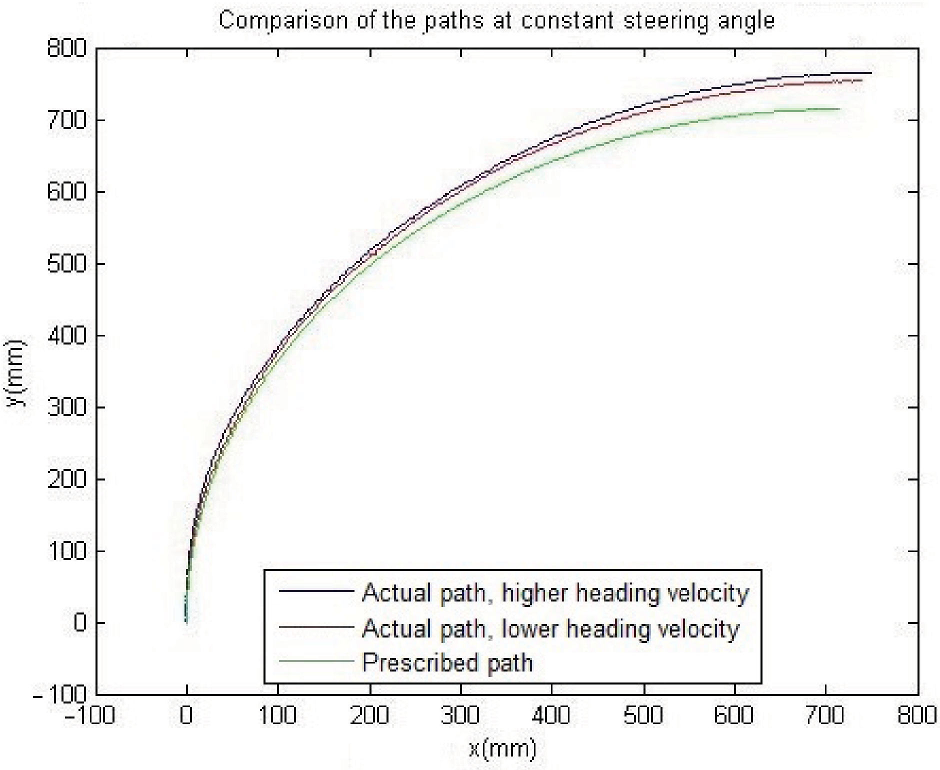

Fig. 3.3 Tests 2 and 3

Test 4, shown in Fig. 3.4, corresponds to a turn at a higher heading velocity and steering angle, compared to tests 2 and 3. We expected a larger error.

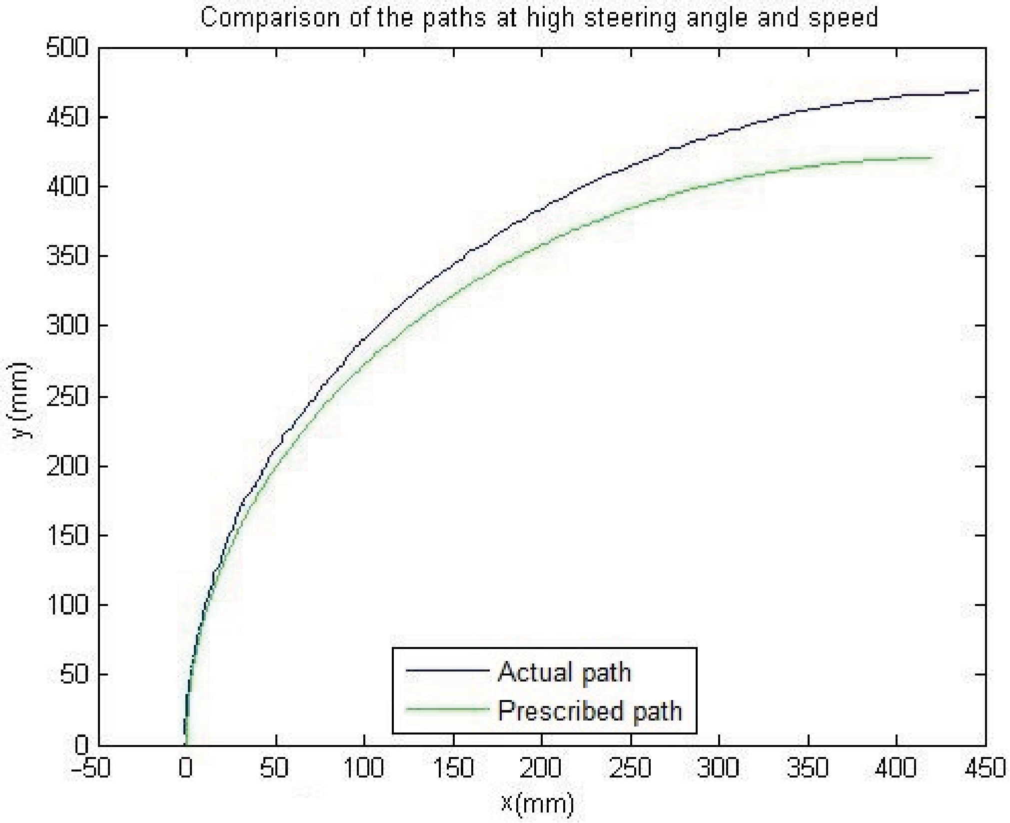

Fig. 3.4 Test 4

3.4 Computation of the Path Error

Of the utmost importance is the path error, between the prescribed, without slippage trajectory, and the actual trajectory. In order to compare the test results, we considered the “path error”, defined as

$$e = \frac{||AB||}{l_c} \tag{3.2}$$

where

A is the end point of the prescribed trajectory,

B is the end point of the actual trajectory, and

l_c is the arc length of the actual trajectory

The length of the actual trajectory that is, the trajectory that we have obtained as a set of points, was computed as the sum of the distances between two successive points. This means we used linear interpolation between measurement points, and we added the lengths of the segments between successive points. The results of the computation are shown in the Table 3.2 below.

Test number	Error (%)
1	3.39
2	3.87
3	5.18
4	10.9

Table 3.2 Path Errors of the Tests

3.5 Analysis of the Results

During the first test, shown in Fig. 3.2, there was some drift, even if the robot is moving on a straight course. The robot tended to veer slightly to the left, but the distance between the last position of the robot and the place where it should stop, is about 0.02 m. As a result, part of the error seen in the next tests was due to this drift, which remained small and was not caused by slipping, since it was observed even when the robot is not turning.

Moreover, the second and third tests, shown in Fig. 3.3, correspond to two turns, at the same steering angle but different heading velocities. We observed a deviation, with the errors being larger than the one observed during test 1. This additional drift was mostly caused by slipping, which increases with speed, as one can see in this figure. Our results are consistent with the expectations: there is some drift at lower speed and heading velocity, part of which is caused by the control system and the rest by dynamic slipping. The prescribed paths shown here rely on the assumption of no slippage, which was never completely satisfied during in the field tests. This assumption did not take into account centrifugal forces and friction. Moreover, as the error remains small, the non-slippage assumption is regarded as relevant at lower speed and lower heading velocity. For these reasons, we were correct to verify the Ackermann conditions at the lower speeds and steering angles of the tests, as in tests 2 and 3.

The next test allowed us to determine whether satisfying the Ackermann conditions at higher steering angle and heading velocity was achieved and to consider the influence of the inputs on the slippage. Figure 3.4 shows the results of the fourth test, where both the heading velocity and the steering angle drastically increase. In this case, there is much slippage, as expected. In fact, the error becomes quite big, with the result that the non-slippage assumption becomes much less relevant. Thus, in this situation, satisfying the Ackermann conditions is not possible, because this strategy does not take into account centrifugal forces. We suggest using an alternative strategy consisting of implementing steering angles and angular velocities that would counteract the slippage. However, researching such possible solutions is a long process, and no suggestion is provided here as it lies beyond the scope of this thesis.

Chapter 4

Dynamics Analysis

Here we investigate possible ways of preventing skidding as the centre of mass of the chassis describes a circular trajectory. Because of the scope of a Master's thesis, the results reported in this chapter were not validated experimentally. The model used here is standard (Coudon, 2006; Guillet, 2011) and gives the general lead about how to improve the prototype. In particular, we derive a grip-limit equality that shows the influence of the friction coefficient in order to conclude on improvements that should be implemented on the prototype.

4.1 Uniformly Accelerated Circular Trajectory

Here are presented well-known expressions of the tangential and normal accelerations while the centre of mass of the chassis traces a circular trajectory under a uniformly accelerated motion, as shown in Fig. 4.1, that will be used in the dynamics analysis. In this figure, $\boldsymbol{a}$ is the acceleration of the centre of mass C of the vehicle, while $\boldsymbol{a}_n$ is its normal and $\boldsymbol{a}_t$ is its tangential component. In all the equations and figures, bold variables represent vector quantities. Expressions of the tangential and normal accelerations are recalled below:

$$||\boldsymbol{a}_n|| = \frac{v^2}{r} \tag{4.1a}$$

$$||\boldsymbol{a}_t|| = \frac{dv}{dt} = a_t \tag{4.1b}$$

$$||\boldsymbol{a}|| = \sqrt{\left(\frac{v^2}{r}\right)^2 + {a_t}^2} \tag{4.1c}$$

where v is the speed of C.

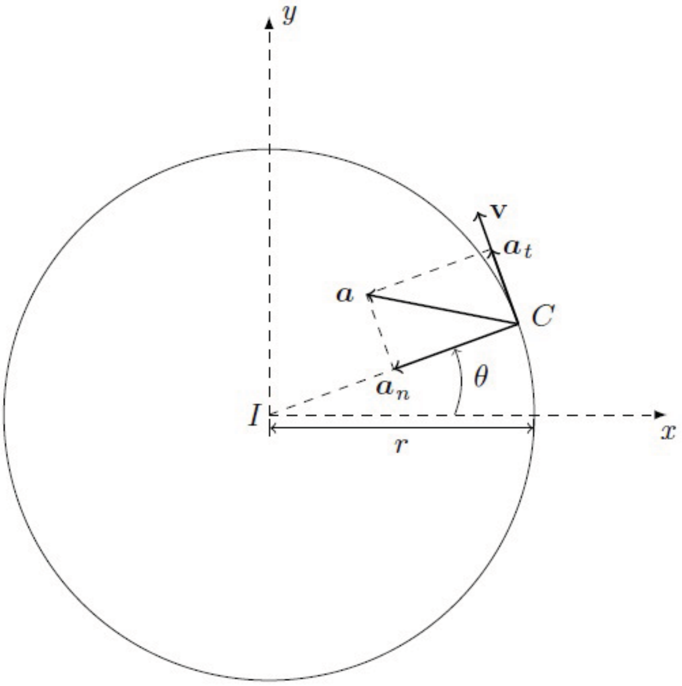

Fig. 4.1 Uniformly accelerated circular trajectory

4.2 Bicycle Model

The bicycle model is the standard simple model to study skidding of automotive vehicles (Baffet, 2006; Pouly, 2011). Here, we modify it slightly, to adapt this model to our prototype, which is a rear-drive vehicle. We first consider the rear part of the car, shown in Fig. 4.2. This part is modelled as the rear wheel of a bicycle, by means of a propelling force $\mathbf{f}_p$ (it is the tangential component of the force applied by the road to the wheels, namely, the reaction of the road), a resulting torque τ and a resulting normal reaction force $\mathbf{f}_n$ of the road. Then we consider the whole vehicle, modeled as shown in Fig. 4.3. In this model $\mathbf{f}_n$ is the normal component of the reaction of the road applied to the rear wheel.

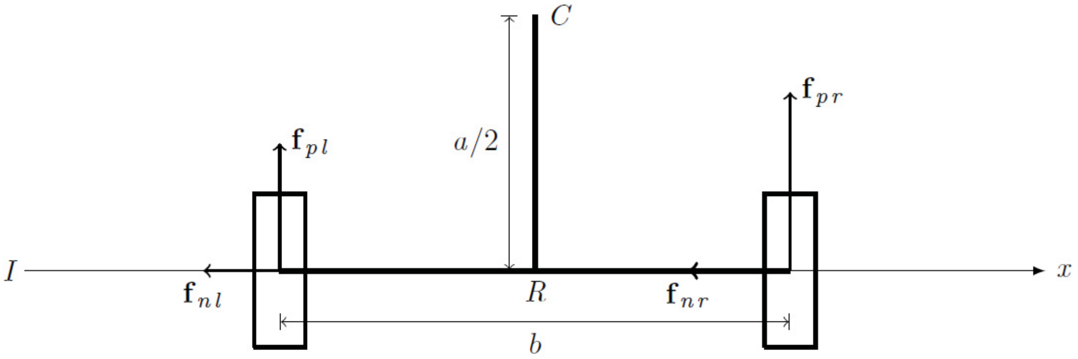

Fig. 4.2 Rear part of the vehicle

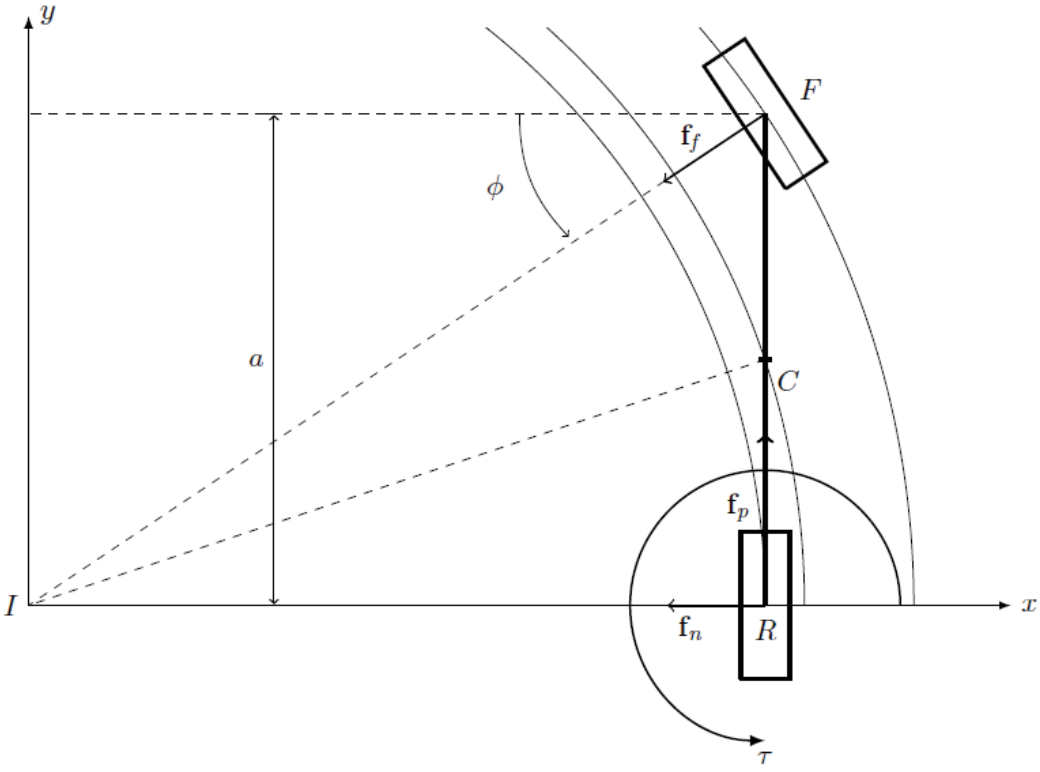

;

Fig. 4.3 Modified bicycle model

$$\mathbf{f}_p = \mathbf{f}_{pr} + \mathbf{f}_{pl} \tag{4.2a}$$

$$||\mathbf{f}_p|| = ||\mathbf{f}_{pr}|| + ||\mathbf{f}_{pl}|| \tag{4.2b}$$

$$\tau = \frac{(||\mathbf{f}_{pr}|| - ||\mathbf{f}_{pl}||)b}{2} \tag{4.2c}$$

In this study, we first derive $||\mathbf{f}_p||$ and τ, then $||\mathbf{f}_{pl}||$ and $||\mathbf{f}_{pr}||$ can be obtained by means of the relations

$$||\mathbf{f}_{pr}|| = \frac{1}{2}\left(\frac{2\tau}{b} + ||\mathbf{f}_p||\right) \tag{4.3a}$$

$$||\mathbf{f}_{pl}|| = \frac{1}{2}\left(||\mathbf{f}_p|| - \frac{2\tau}{b}\right) \tag{4.3b}$$

Since the motion is planar, the Newton-Euler equations yield

$$\mathbf{f} = m\boldsymbol{a} \tag{4.4a}$$

$$T = J_z\dot{\omega}$$

where $\mathbf{f}$ is the resulting horizontal force (i.e. in the plane of motion, hence the weight is excluded as a force normal to this plane), T is the resulting torque w.r.t. the centre of mass, and $\dot{\omega}$ the angular acceleration of the vehicle. Moreover,

$$\mathbf{f} = \mathbf{f}_p + \mathbf{f}_n + \mathbf{f}_f \tag{4.5a}$$

$$T = \frac{(||\mathbf{f}_f||\cos\phi - ||\mathbf{f}_n||)a}{2} + \tau \tag{4.5b}$$

where $\mathbf{f}_f$ is the force applied by the ground to the front wheel. The Newton-Euler equations thus yield

$$ma_x = -||\mathbf{f}_n|| - ||\mathbf{f}_f||\cos\phi \tag{4.6a}$$

$$ma_y = ||\mathbf{f}_p|| - ||\mathbf{f}_f||\sin\phi \tag{4.6b}$$

$$J_z\dot{\omega} = \frac{(||\mathbf{f}_f||\cos\phi - ||\mathbf{f}_n||)a}{2} + \tau \tag{4.6c}$$

Besides, we introduce φ to simplify expressions

$$\varphi = \arctan\left(\frac{\tan\phi}{2}\right) \tag{4.7}$$

Moreover, the angular velocity ω and angular acceleration are readily derived as

$$\omega = \frac{v}{r} = \frac{v \tan\phi}{a} \tag{4.8a}$$

$$\dot{\omega} = \frac{1}{r}\frac{dv}{dt} = \frac{a_t}{r} \tag{4.8b}$$

Hence, $\dot{\omega}$ is known. Furthermore, before the vehicle starts to skid, a_n and a_t are known. Moreover, a_x and a_y can be expressed as

$$\boldsymbol{a} = \boldsymbol{a}_n + \boldsymbol{a}_t \tag{4.9a}$$

$$\begin{aligned} a_x &= -a_n \cos\varphi - a_t \sin\varphi \\ &= -\frac{v^2}{r}\cos\varphi - a_t \sin\varphi \end{aligned} \tag{4.9b}$$

$$\begin{aligned} a_y &= -a_n \sin\varphi + a_t \cos\varphi \\ &= -\frac{v^2}{r}\sin\varphi + a_t \cos\varphi \end{aligned} \tag{4.9c}$$

After a study of grip-limit, we will limit ourselves to skidding motions of the vehicle that make the centre of mass undergo a motion outside of its prescribed trajectory. During skidding, at least one rear wheel will also go outside of its prescribed trajectory, because the positions of the two rear wheels give the position of the chassis centre of mass since the latter is modelled as a rigid body.

4.2.1 Grip-limit

At grip-limit, an additional equation is obtained by using the Coulomb law applied to whole vehicle

$$\frac{||\mathbf{f}||}{||\mathbf{n}||} = \mu_s \tag{4.10}$$

where

$\mathbf{f}$:	Resulting tangential force applied by the road to the vehicle
$\mathbf{n}$:	Resulting normal reaction force applied by the road to the vehicle
μ_s:	Static friction coefficient between the wheels and the road

In the model that was adopted, $\mathbf{f}_t$ has already been expressed in terms of the unknowns as

$$\mathbf{f} = \mathbf{f}_p + \mathbf{f}_n + \mathbf{f}_f \tag{4.11}$$

With regards to the normal force, since the vehicle sticks to the horizontal ground with no vertical acceleration and a planar rotation in (I, x, y), $\mathbf{n}$ is readily found as

$$||\mathbf{n}|| = mg \tag{4.12}$$

Hence the grip-limit equation can be written as,

$$||\mathbf{f}||^2 = m^2a^2 = m^2({a_n}^2 + {a_t}^2) = (\mu_s mg)^2 \tag{4.13}$$

$$\frac{v^4}{r^2} + {a_t}^2 = {\mu_s}^2 g^2 \tag{4.14}$$

This grip limit equality means that, for any steering angle, there exists a maximum acceleration that the vehicle can reach without skidding. In particular, we observe that if the heading acceleration is equal to zero (i.e. $a_t = 0$, a uniform rotation) there exists a maximum pure rolling heading velocity v which depends on the steering angle only, since the rotation radius r also depends only on the steering angle. A plot of the maximum velocity of a vehicle that is not skidding during a uniform rotation (i.e., $a_t = 0$) versus the radius of the rotation, with different materials and tires in contact, is shown in Fig. 4.4.

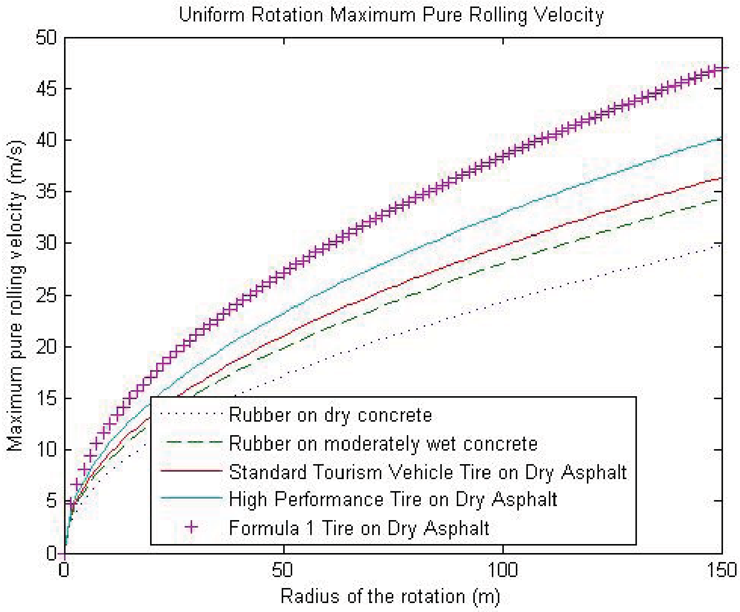

Fig. 4.4 Maximum pure rolling velocity of a vehicle (source of the friction coefficients: http://hpwizard.com/)

The results found in this section are consistent with what can be found in the literature (Blundell and Harty, 2004): “The minimum radius available in normal driving is the turning circle. At higher speeds the limit to path curvature is not the amount [by which] the wheels can be turned[,] but rather the maximum centripetal force that can be generated. This is governed by the limiting coefficient of friction μ between tyres and road, typically around 0.9. Simplistically, if friction is independent of [the contact] area (the Newtonian model), the theoretical maximum centripetal acceleration [...] is identical to the friction coefficient, μ :

$$\frac{A_y}{g} = \frac{F_y}{mg} = \frac{mg\mu}{mg} = \mu\text{''}$$

Moreover, if the heading velocity of the car is smaller than the maximum heading velocity, there exist a non-null maximum tangential acceleration (given via the pedals of the vehicle) for a pure rolling turn. Furthermore, "The static friction coefficient depends on speed and the condition of tires and road." (Avallone, 2007). We will not consider here wet pavement, where aquaplaning may occur "on wet pavement, the coefficient falls even more, especially at high speeds". An approximate value of μ_s is 1, for a vehicle that is moving on dry concrete, and whose wheels are made of rubber.

Derivation of the Forces at Grip-limit during Uniform Turning

Here we investigate the uniform turning, i.e., under $a_t = 0$. Besides, since the centre of mass of the vehicle is halfway between the front and rear wheels, the same weight, half of the total weight, lies on each couple of wheels. Thus, we assume that both wheels of the bicycle model create the same normal resisting force, i.e. $||\mathbf{f}_f|| = ||\mathbf{f}_n||$. In this case, the Newton-Euler equations yield

$$a_n = \mu_s g \tag{4.15a}$$

$$-ma_n \cos\varphi = -||\mathbf{f}_n||(1+\cos\phi) \tag{4.15b}$$

$$-ma_n \sin\varphi = ||\mathbf{f}_p|| - ||\mathbf{f}_f|| \sin\phi \tag{4.15c}$$

$$0 = \tau - \frac{||\mathbf{f}_f||(1-\cos\phi)a}{2} \tag{4.15d}$$

Hence, one readily obtains the norms of these forces and torque at limit of grip, which we will distinguish from their skidding values by means of 0 subscripts as

$$||\mathbf{f}_f||_0 = ||\mathbf{f}_n||_0 = \frac{m\mu_s g \cos\varphi}{1+\cos\phi} \tag{4.16a}$$

$$||\mathbf{f}_p||_0 = m\mu_s g\left(\frac{\sin\phi\cos\varphi}{1+\cos\phi} - \sin\varphi\right) \tag{4.16b}$$

$$\tau_0 = m\mu_s g\cos\varphi\left(\frac{1-\cos\phi}{1+\cos\phi}\right)\frac{a}{2} \tag{4.16c}$$

where we recall

$$\varphi = \arctan\left(\frac{\tan\phi}{2}\right)$$

Furthermore, another notation is introduced for the derivations of the next subsection as

$$f_{x0} = -||\mathbf{f}_n||_0(1+\cos\phi) = -ma_n\cos\varphi = -mg\mu_s\cos\varphi \tag{4.17a}$$

$$f_{y0} = ||\mathbf{f}_p||_0 - ||\mathbf{f}_f||_0\sin\phi = -ma_n\sin\varphi = -mg\mu_s\sin\varphi \tag{4.17b}$$

$$T_0 = \tau_0 - \frac{||\mathbf{f}_f||_0(1-\cos\phi)a}{2} = 0 \tag{4.17c}$$

4.2.2 Incipient Skidding

Here is considered the vehicle just after it starts skidding. The model below is used to study the onset of skidding. To this end, the bicycle model is altered, as shown in Fig. 4.5. We use the inertial frame whose centre is the instant centre of rotation of the vehicle at limit of grip; and such that at $t = 0$ we have $\theta = 0$ and the vehicle starts to skid.

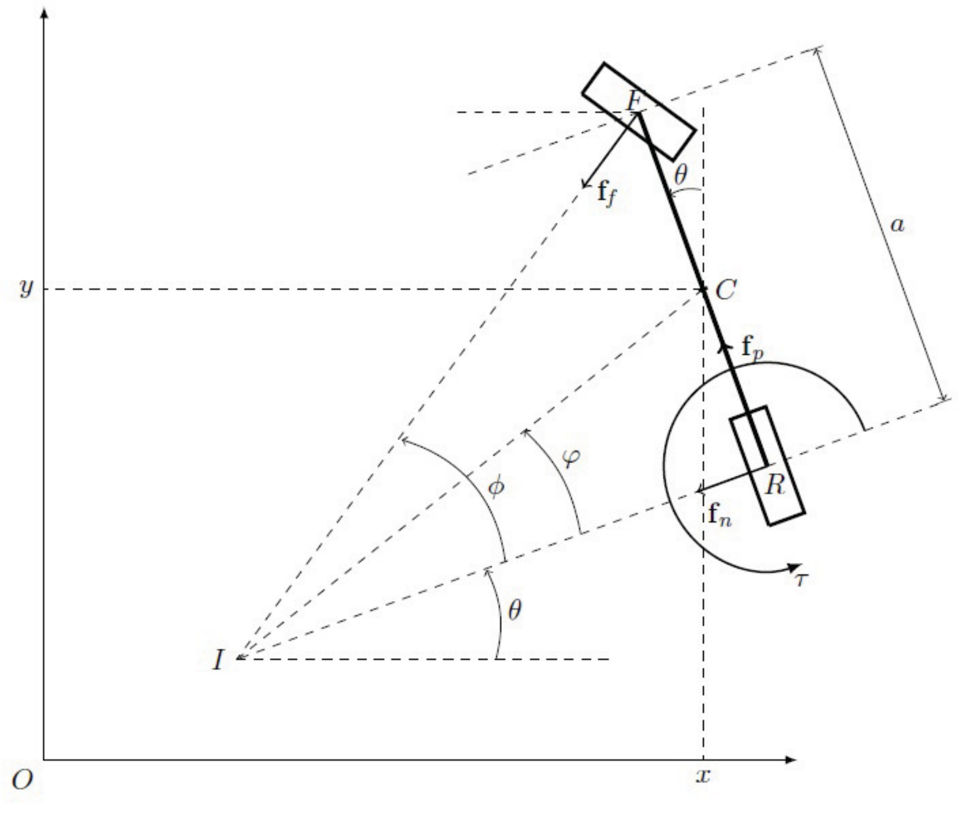

Fig. 4.5 Bicycle Model Applied to a Skidding Vehicle

In this study, we assume that the propelling force $\mathbf{f}_p$, the propelling torque τ and the normal reaction forces $\mathbf{f}_n$ and $\mathbf{f}_f$ are known and have constant norms. It is assumed that these forces are equally altered by the sudden change of friction coefficient when the vehicle starts to skid (from the static value just before skidding to the dynamic value once skidding has started). Thus, we assume that their norms during the onset of skidding are constant and proportional to their values at the limit of grip, the proportionality coefficient being μ_d/μ_s. Or, equivalently, μ_d is substituted by μ_s in expressions (4.16). Hence,

$$||\mathbf{f}_f|| = ||\mathbf{f}_n|| = \frac{\mu_d}{\mu_s}||\mathbf{f}_f||_0 = \frac{\mu_d}{\mu_s}||\mathbf{f}_n||_0 = \frac{\mu_d}{\mu_s}\frac{m\mu_s g\cos\varphi}{1+\cos\phi} = \frac{m\mu_d g\cos\varphi}{1+\cos\phi} \tag{4.18a}$$

$$||\mathbf{f}_p|| = \frac{\mu_d}{\mu_s}||\mathbf{f}_p||_0 = \frac{\mu_d}{\mu_s}m\mu_s g\left(\frac{\sin\phi\cos\varphi}{1+\cos\phi} - \sin\varphi\right) = m\mu_d g\left(\frac{\sin\phi\cos\varphi}{1+\cos\phi} - \sin\varphi\right) \tag{4.18b}$$

$$\tau = \frac{\mu_d}{\mu_s}\tau_0 = \frac{\mu_d}{\mu_s}m\mu_s g\cos\varphi\left(\frac{1-\cos\phi}{1+\cos\phi}\right)\frac{a}{2} = m\mu_d g\cos\varphi\left(\frac{1-\cos\phi}{1+\cos\phi}\right)\frac{a}{2} \tag{4.18c}$$

The unknowns are

x, y : Coordinates of the centre of mass,

θ : Angle of rotation of the chassis

and their time derivatives. Here the Newton-Euler equations give

$$m\ddot{x} = -||\mathbf{f}_f||\cos(\theta+\phi) - ||\mathbf{f}_n||\cos\theta - ||\mathbf{f}_p||\sin\theta \tag{4.19a}$$

$$= -||\mathbf{f}_f||\cos\theta\cos\phi + ||\mathbf{f}_f||\sin\theta\sin\phi - ||\mathbf{f}_n||\cos\theta - ||\mathbf{f}_p||\sin\theta \tag{4.19b}$$

$$m\ddot{y} = -||\mathbf{f}_f||\sin(\theta+\phi) - ||\mathbf{f}_n||\sin\theta + ||\mathbf{f}_p||\cos\theta \tag{4.19c}$$

$$= -||\mathbf{f}_f||\sin\theta\cos\phi - ||\mathbf{f}_f||\cos\theta\sin\phi - ||\mathbf{f}_n||\sin\theta + ||\mathbf{f}_p||\cos\theta \tag{4.19d}$$

$$J_z\dot{\omega} = \frac{(||\mathbf{f}_f||\cos\phi - ||\mathbf{f}_n||)a}{2} + \tau \tag{4.19e}$$

where we recall

$$\varphi = \arctan\frac{\tan\phi}{2}$$

Moreover, by plugging equations (4.18) into (4.19)

$$m\ddot{x} = \frac{\mu_d}{\mu_s}\left(-||\mathbf{f}_f||_0\cos\theta\cos\phi + ||\mathbf{f}_f||_0\sin\theta\sin\phi - ||\mathbf{f}_n||_0\cos\theta - ||\mathbf{f}_p||_0\sin\theta\right) \tag{4.20a}$$

$$m\ddot{y} = \frac{\mu_d}{\mu_s}\left(-||\mathbf{f}_f||_0\sin\theta\cos\phi - ||\mathbf{f}_f||_0\cos\theta\sin\phi - ||\mathbf{f}_n||_0\sin\theta + ||\mathbf{f}_p||_0\cos\theta\right) \tag{4.20b}$$

$$J_z\dot{\omega} = \frac{\mu_d}{\mu_s}\left(\frac{(||\mathbf{f}_f||_0\cos\phi - ||\mathbf{f}_n||_0)a}{2} + \tau_0\right) \tag{4.20c}$$

Then, by injecting equations (4.17) in (4.20)

$$m\ddot{x} = \frac{\mu_d}{\mu_s}\left(f_{x0}\cos\theta - f_{y0}\sin\theta\right) = \frac{\mu_d}{\mu_s}\mu_s mg(\sin\varphi\sin\theta - \cos\varphi\cos\theta) \tag{4.21a}$$

$$m\ddot{y} = \frac{\mu_d}{\mu_s}\left(f_{x0}\sin\theta + f_{y0}\cos\theta\right) = \frac{\mu_d}{\mu_s}\mu_s mg(-\sin\varphi\cos\theta - \cos\varphi\sin\theta) \tag{4.21b}$$

$$J_z\dot{\omega} = \frac{\mu_d}{\mu_s}T_0 = 0 \tag{4.21c}$$

Thus,

$$\ddot{x} = -\mu_d g\cos(\theta + \varphi) \tag{4.22a}$$

$$\ddot{y} = -\mu_d g\sin(\theta + \varphi) \tag{4.22b}$$

$$\dot{\omega} = 0 \tag{4.22c}$$

4.2.3 Simulation

Matlab is used to simulate skidding. Equations (4.22) are used and the parameters of the simulation are shown in Table 4.1. Before skidding, we assume that the vehicle undergoes a uniform turning, at a given steering angle and at the constant grip-limit velocity corresponding to this steering angle. We assume the prototype starts skidding at $y = 0$, at an initial vertical and upward velocity equal to the maximum pure rolling velocity at this steering angle. Or, equivalently, we choose an inertial frame such that this assumption is true. Hence, we simulate the X-by-wire vehicle under conditions similar to the tests described in Chapter 3, except for the material of the wheels, since we assume proper rubber wheels. Then we modify the dynamic friction coefficient, once it is increased and once it is decreased w.r.t. its value for the wheels that are currently used.

Parameter	Symbol	Value
Wheel base	a	0.48 m
Mass	m	19.5 kg
Planar moment of inertia	J_z	0.71 kg/m^2
Coefficient of static friction	μ_s	1.0
Standard Coefficient of kinetic friction	μ_d	0.8
Increased Coefficient of kinetic friction	μ_d	0.9
Decreased Coefficient of kinetic friction	μ_d	0.7
Steering angle	ϕ	0.61 rad
Initial and grip-limit velocity	v_0	2.6 m/s

Table 4.1 Simulation parameters of the main simulation

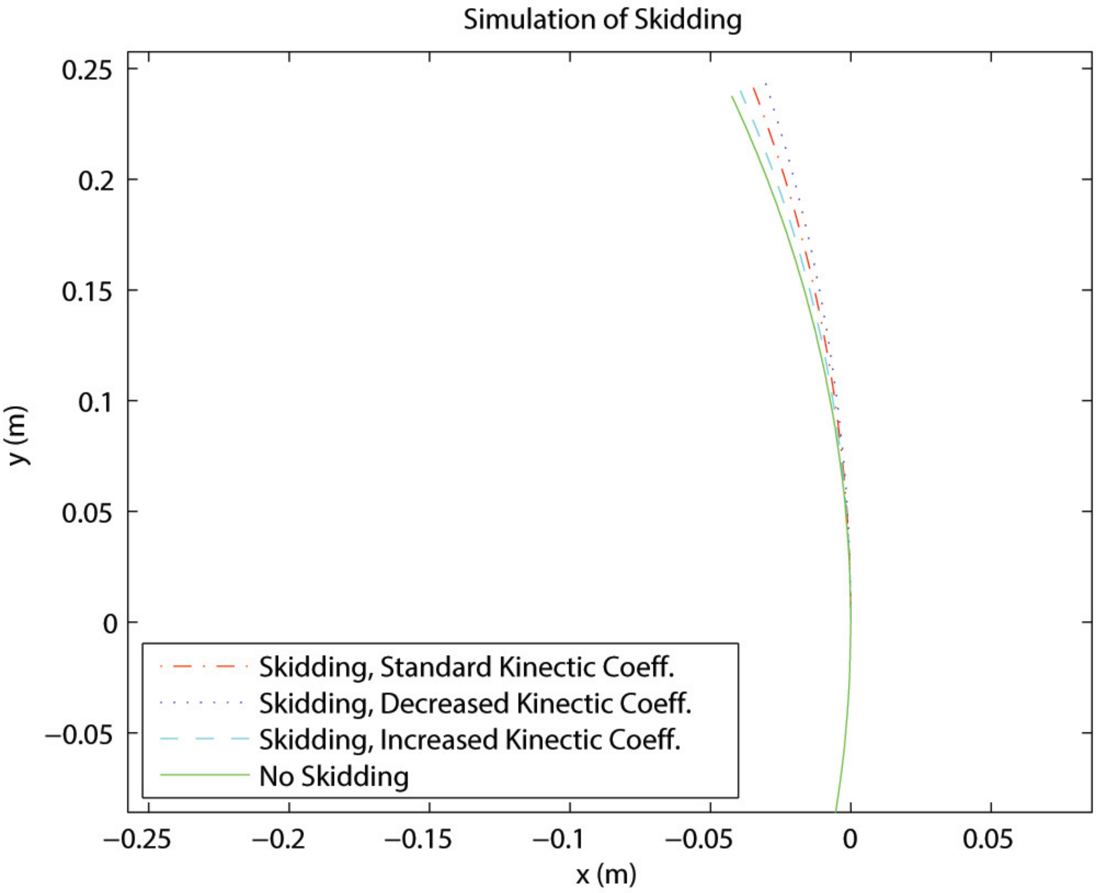

Fig. 4.6 Skidding simulations with different kinetic friction coefficients

The kinetic friction coefficient has a significant impact on skidding behaviour. We can see in Fig. 4.6 that higher coefficients lead to smaller drifts. The kinetic friction coefficients used are 0.7, 0.8 and 0.9. This is why the wheels of the Formula 1 vehicles have high friction coefficients, even greater than 1.

4.2.4 Conclusion

We conclude that the friction coefficient should be made as high as possible in order to limit skidding. This can be easily done with the prototype presented in here, by adding a layer of a material that has an higher friction coefficient with the floor. The contact surfaces of the wheels should also be altered, for example by adding anti-slip patterns.

Chapter 5

Closing Remarks

5.1 Conclusions

As reported in this thesis, a full X-by-wire automotive prototype was designed and tested. The state of the art of by-wire technologies was first explored, by comparing them to those of the standard mechanical automotive architectures. Additionally, kinematic and geometric Ackermann conditions were cast in a form suitable to X-by-wire technologies. These conditions correspond to the kinematically correct turning; it cannot be satisfied with any mechanical architecture. Relevant technical requirements and aims were set to define the scope of the thesis work, as well as the characteristics of a full X-by-wire proof-of-concept prototype.

The complete design process, from the conceptual design to the detailed design, including the mechanical and electronic subsystems, was explained. The mechanical structure comprises a robust aluminum chassis, a front steering mechanism, a rear traction structure and a box to house the battery. The details of these mechanisms were discussed; the way they are connected together was also described. With regard to the electronics, the overall structure using a steering wheel, pedals, LabVIEW, Arduino and smart control cards was discussed. The LabVIEW control system, which receives the steering and speed commands from a Logitech steering wheel and pedals kit, processes the data. LabVIEW is used not only to implement the computations, but also for its safety features. Furthermore, the role of the Arduino Mega board as an embedded control system was discussed, followed by an explanation of the capabilities of the control cards. The outputs of the motors (angular velocity and position) were maintained equal to their reference signals, as sent by the Arduino board, using the feedback controllers implemented in their control cards. The four motors of the prototype were shown, and their selection was explained.

The methodology and results of the tests were then discussed. The Vicon motion-capture system was used to track the trajectory of the vehicle. The principle of this system was described, prior to explaining the rationale behind the tests and a discussion of the results. These tests have shown that the prototype works within a small error tolerance along a straight line. The assumption of non-slippage, used to generate the prescribed paths when the prototype turns, is relevant at low speeds and steering angles (when the inertial forces are negligible). However, this assumption no longer holds at higher values because of the skidding, caused by strong centrifugal forces. The effects of these two inputs on the path error, compared to the prescribed path, were analyzed. The errors are not that significant, considering that the system is generally open-loop and that it uses only a single-behaviour algorithm that does not adapt to the inputs. Furthermore, the model implemented in this algorithm should be used only at low speed and steering angle (when the inertial forces are negligible). A provision must be made, with feedback control, to ensure that the Ackermann conditions are observed under higher inertial forces.

Afterward, a dynamics model was created and analyzed, to investigate possible methods to prevent or limit skidding. The model shows that the static and kinetic friction coefficients have a great impact on skidding, and should be made as high as possible, through the choice and improvements of the wheels.

We conclude that X-by-wire architectures can be implemented in automotive vehicles. Although implementation requires further development, the proof-of-concept prototype shows that the X-by-wire architecture is feasible, that X-by-wire vehicles should be feasible in the foreseeable future.

5.2 Recommendations for Further Research

As an extension to the research work reported in this thesis, several issues remain to be studied, while additional capabilities should be implemented:

- First and foremost, more elaborate dynamics models should be introduced and the prototype should undergo further tests. When implementing more complex models, slippage angles and path errors should be accounted for, depending on the control inputs and friction coefficients. These parameters should, in turn, be experimentally validated, so that the influence of heading velocity and steering angle on the path error can be further assessed.
- The wheels of the prototype must be upgraded, to increase the friction coefficients, in order to reduce or suppress skidding.
- A larger and safer test area should be used to test the prototype at higher speeds and heading velocities than those used during the work described here. Regarding the mechanical structure, elaborate suspensions can be implemented, including inclined and active suspensions, by taking into account the vehicle dynamics. Heuristic algorithms could be used to improve the dynamics of the prototype, in particular when the prototype faces strong centrifugal forces.
- In addition, pose data measured by the Vicon system could be used to correct in real time the path of the prototype. This will make the overall control system closed-loop.
- Even though XBee modules were installed, a robust wireless connection could not be established because of complex technical issues. Such a connection would increase the capabilities of the prototype, which currently relies on a long wire for its control.
- Many kinds of parking or emergency algorithms can be implemented and tested, including algorithms for preventing automobile crashes. Furthermore, by means of additional sensors including cameras,

path-tracking algorithms, or even automatic control algorithms, can be implemented that would make the vehicle fully autonomous.

APPENDIX: Arduino Code

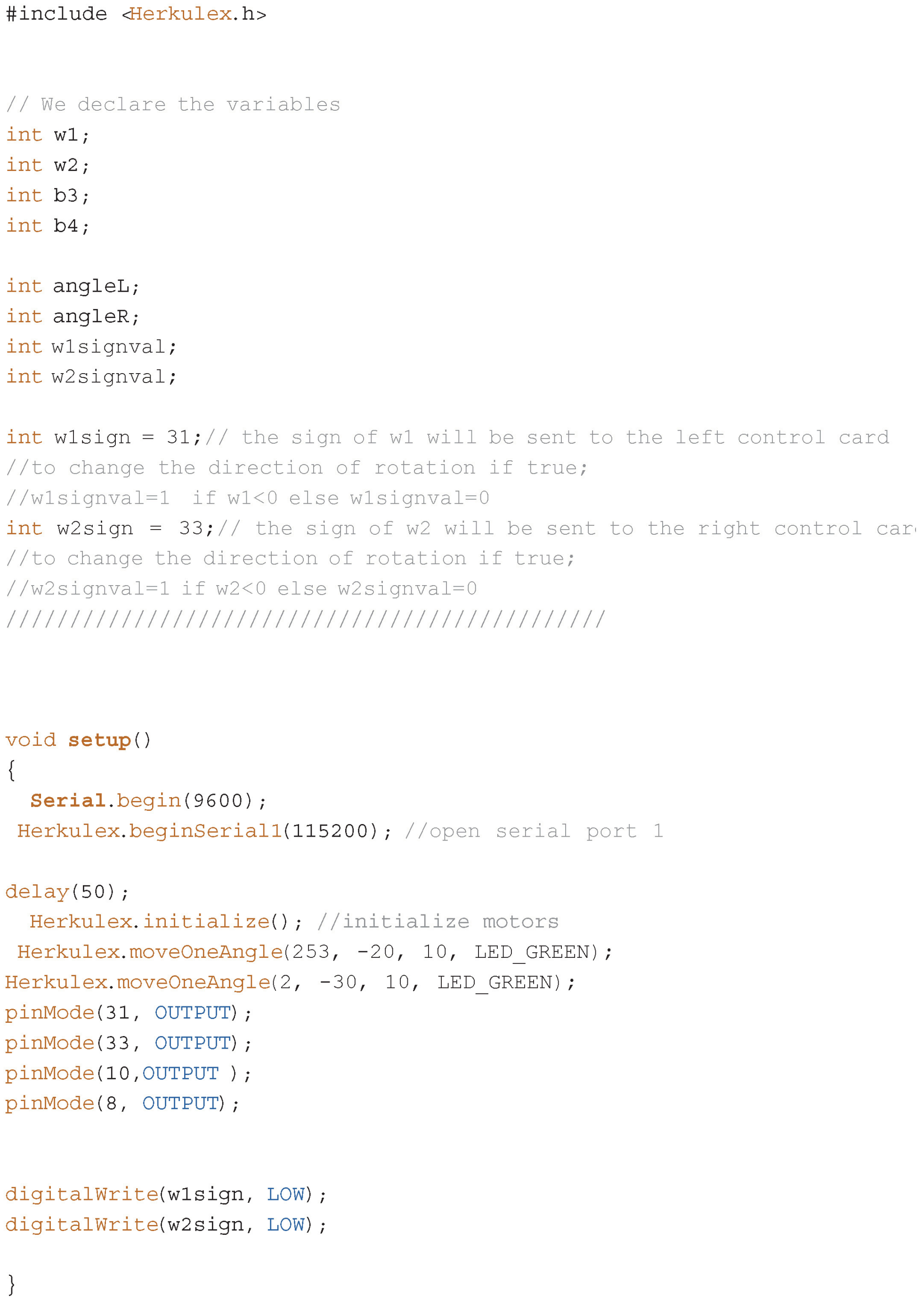

```
#include <Herkulex.h>


// We declare the variables
int w1;
int w2;
int b3;
int b4;

int angleL;
int angleR;
int w1signval;
int w2signval;

int w1sign = 31;// the sign of w1 will be sent to the left control card
//to change the direction of rotation if true;
//w1signval=1  if w1<0 else w1signval=0
int w2sign = 33;// the sign of w2 will be sent to the right control car
//to change the direction of rotation if true;
//w2signval=1 if w2<0 else w2signval=0
///////////////////////////////////////////////



void setup()
{
  Serial.begin(9600);
 Herkulex.beginSerial1(115200); //open serial port 1

delay(50);
  Herkulex.initialize(); //initialize motors
 Herkulex.moveOneAngle(253, -20, 10, LED_GREEN);
Herkulex.moveOneAngle(2, -30, 10, LED_GREEN);
pinMode(31, OUTPUT);
pinMode(33, OUTPUT);
pinMode(10,OUTPUT );
pinMode(8, OUTPUT);


digitalWrite(w1sign, LOW);
digitalWrite(w2sign, LOW);

}
```

Fig. 1 Arduino code, page 1/3 (initialization function)

```
void loop()

{
 //If we received 6 instructions we open the loop
////////////////////////////////////////////////
 if (Serial.available() == 6) {

w1=Serial.read();
w2=Serial.read();
b3=Serial.read();//b3 is phi 1
b4=Serial.read();//b4 is phi 2
w1signval=Serial.read();
// w1signval=1 if w1<0, w1signval=0 if w1>=0
w2signval=Serial.read();
// w2signval=1 if w2<0, w2signval=0 if w2>=0

//A subloop to give the directions
////////////////////////////////////////////////

/to the two control cards
if (w1signval==1)
{digitalWrite(w1sign, HIGH);}
else
{digitalWrite(w1sign, LOW);}
if (w2signval==1)
{digitalWrite(w2sign, HIGH);}
else
{digitalWrite(w2sign, LOW);}



//The rear motors' angular velocities target values
//are sent to the control cards
////////////////////////////////////////////////
analogWrite(8,w1);//
analogWrite(10,w2);

//The real speed feedbacks from the control cards
//are received and mapped to 0-255 for transmission to labview
////////////////////////////////////////////////
int w1feedback=analogRead(1);
int w2feedback=analogRead(2);

w1feedback=map(w1feedback,0,1024,0,255);
w2feedback=map(w2feedback,0,1024,0,255);
```

Fig. 2 Arduino code, page 2/3 (main loop, page 1/2)

```
//Transmssion of the angular velocities' feedback
///////////////////////////////////////////////
Serial.write(w1feedback);
Serial.write(w2feedback);




//Mappings and transmissions of the front angles' references
//to the Herkulex servo motors
///////////////////////////////////////////////
b3=map(b3,0,255,-60,85);//mappings for moveOneAngle
b4=map(b4,0,255,-85,60);


Herkulex.moveOneAngle(253, -b3-20, 10, LED_BLUE);
Herkulex.moveOneAngle(2, -b4-30, 10, LED_BLUE);

//Feedback from the front servos and mappings
//for transmission to the laptop
///////////////////////////////////////////////
int angle1=Herkulex.getPosition(1);
//if we use get position to obtain the angle
int angle2=Herkulex.getPosition(2);
 angle1=map(angle1,0,1024,0,255);
//mappings for front servos angles with getPosition
angle2=map(angle2,0,1024,0,255);

Serial.write(angle1);
Serial.write(angle2);


}
```

Fig. 3 Arduino code, page 3/3 (main loop, page 2/2)

References

J. Ackermann, T. Bunte, and D. Odenthal. Advantages of active steering for vehicle dynamics control. *I99ME013*, 1999.

S. Amberkar. A control system methodology for steer-by-wire systems. *SAE Technical Paper Series*, 2004-01-1106, 2004.

B. Andonian. Steer-by-wire system with steering feedback, Patent US 20020079155 A1, 2001.

J. Angeles. *Rational Kinematics*. Springer, 1988.

J. Angeles. *MECH 577 Optimum Design Lecture Notes*. McGil University Course Lecture Notes, available on http://www.cim.mcgill.ca/ rmsl/Index/Documents/MECH577/LN110614.pdf, Montreal, Canada, 2011a.

J. Angeles. *Dynamic Response of Linear Mechanical Systems: Modeling, Analysis and Simulation*. Springer, 2011b.

S. Anwar. *Fault Tolerant Drive By Wire Systems: Impact on Vehicle Safety and Reliability*. Bentham books, 2012.

E. Avallone. *Marks' Standard Handbook for Mechanical Engineers*. McGraw Hill, 2007.

G. et al. Baffet. Estimation de lâĂŹangle de dťerive et des efforts latťeraux dâĂŹun vťehicule dans des situations de conduites standards ou critiques : simulations et expťerimentations. Bordeaux, France, 2006. Confťerence Internationale Francophone dâĂŹAutomatique.

R. Bitter, T. Mohiuddin, and M. Nawrocki. *LabVIEW Advanced Programming Techniques*. CRC press, Taylor and Francis Group, 2007.

M. Blundell and D. Harty. *The Multibody Systems Approach to Vehicle Dynamics*. Elsevier Butterworth Heinemann, 2004.

R.G. Budynas and J.K. Nisbett. *Shigley's Mechanical Engineering Design Ninth Edition*. McGraw Hill, 2008.

C. Carlson and J. Gerdes. Optimal rollover prevention with steer-by-wire and differential braking, 2003.

A. Chevalier. *Guide du Dessinateur Industriel*. Hachette Technique, 2004.

R. P. G. Collinson. *Introduction to Avionics Systems,third Edition*. Springer, 2011.

J. et al. Coudon. A new reference model for steer-by-wire applications with embedded vehicle dynamics. Minneapolis, MN, USA, 2006. American Control Conference.

D. A. Crolla. *Automotive Engineering Powertrain, Chassis System and Vehicle Body.* Elsevier, 2009.

E. Dilger. Steer-by-wire steering system for motorized vehicles, US Patent 6219604 B1, 2001.

J. Eder and A. Knoll. Yaw rate control of electric vehicle using steer-by-wire system, 2010.

J. Guillet. *E tude et rťeduction dâĂŹordre de modèles linťeaires structurťes Application à la dynamique du vťehicule.* PhD thesis, Université de Haute-Alsace, France, 2011.

A. Hac, D. Doman, and M. Oppenheimer. Unified control of brake- and steer-by-wire systems using optimal control allocation methods. *SAE Technical Paper Series*, 2006-01-0924, 2006.

R. Hayama and K. Nishizaki. The vehicle stability control responsibility improvement using steer-by-wire, 2000.

M. Hosaka and T. Murakami. Yaw rate control of electric vehicle using steer-by-wire system, 2004.

J. S. Im, F. Ozaki, M. Matsunaga, and S. Kawajii. Design of steer-by-wire system with bilateral control method using disturbance observer, 2007.

R.C. Juvinall and K. Marshek. *Fundamentals of Machine Component Design.* John Wiley and Sons, Inc, NYC, USA, 2012.

C. Kelber and D. Webber. Active steering unit with integrated acc for x-by-wire vehicles using a joystick as h.m.i., 2004.

N. Kelling and P. Leteinturier. X-by-wire: Opportunities, challenges and trends. *SAE Technical Paper*, Chemnitz University of Technology, Operating Systems Group, 2003.

S. Laws. Steer-by-wire suspension and steering design for controllability and observability. *IFAC*, 2005.

G. Leen. Expanding automotive electronic systems. *Computer*, Vol. 35, Issue 1, 2002.

M. Margolis. *Arduino Cookbook.* O'Reilly (Ed.), 2012.

W. Mitchell, A. Staniforth, and I. Scott. Analysis of ackermann steering geometry. *SAE Technical Paper Series*, 2006-01-3638, 2006.

H. Naunheimer. *Automotive Transmissions Fundamentals, Selection, Design and Application.* Springer, 2011.

E. Oberg. *Machinery's Handbook 28th edition.* Industrial Press, NYC, USA, 2008.

S. W. Oh, H. C. Chae, and S. C. Yun. The design of a controller for the steer-by-wire system. *JSME International*, Serie C, Vol 47, NO. 3, 2004.

R. Pastorino. Validation of a multibody model for an x-by-wire vehicle prototype through field testing, 2011.

D. Peter and R. Gerhard. Electric power steering: The first step on the way to steer by wire. *SAE Tech. Paper*, 01-0401, 1999.

G. Pouly. *Analysis and synthesis of advanced control laws for vehicle ground guidance.* PhD thesis, Université de Haute-Alsace, France, 2011.

W. Redmond. Fly-by-wire, 1972.

N. Santon and P. Marsden. From fly-by-wire to drive-by-wire: Safety implications of automation in vehicles. *Safety Science*, Vol. 24, Issue 1:Pages 35–49, 1996.

F. Seidel. X-by-wire, 2009.

P. Setlur. Nonlinear tracking controller design for steer-by-wire automotive systems, 2002.

B. Siciliano and O. (editors) Khatib. *Handbook of Robotics*. Springer, Berlin-Heidelberg, 2008.

C. Wilwert. *Design of automotive X-by-wire systems*. Author manuscript, published in *The Industrial Communication Technology Handbook*, Richard Zurawski (Ed.)., 2005.

I. Y. Wong. *Theory of Ground Vehicles*. John Wiley and Sons, Inc., NYC, USA, 2001.

H. Xiaoping and M. Jinming. Proof on impossibility for any plane trapezoid linkage to reproduce ackermann steering exactly. *Transactions of The Chinese Society of Agricultural Machinery*, 2003-06, 2003.

Y. Xu. *Hybrid Electric Vehicle Design and Control: Intelligent Omnidirectional Hybrids*. McGraw Hill, 2014.

Y. Yao. Vehicle steer-by-wire system control. *SAE Technical Paper Series*, 2006-01-1175, 2006.

P. Yih. *Steer-by-wire: Implications For Vehicle Handling and Safety*. PhD thesis, Department of Mechanical Engineering, Stanford University, Stanford, CA, USA, 2005.

P. Yih and C. Gerdes. Steer-by-wire for vehicle state estimation and control, 2004.

P. Yih and C. Gerdes. Modification of vehicle handling characteristics via steer-by-wire. *IEEE Transactions on Control Systems Technology*, Vol. 13, NO. 6, 2005.

B. Zheng. Fault tolerant steer-by-wire road wheel control system. Portland, OR, USA, 2005. American Control Conference.